Ultimate shear behaviour of hybrid reinforced concrete beam-to-steel column assemblages

D.V. Bompa, A.Y. Elghazouli *

Department of Civil and Environmental Engineering, Imperial College London, UK

ABSTRACT

This paper examines the shear transfer mechanisms and ultimate behaviour of hybrid systems consisting of reinforced concrete beams connected to structural steel columns. A series of five large scale tests on structural assemblages, in which steel shear-arms are welded directly to the steel columns and embedded in the reinforced concrete beams, is presented. After describing the experimental arrangement and specimen details, the main results and observations obtained from the tests are provided and discussed. The test results offer a direct evaluation of the ultimate shear behaviour of such hybrid systems. The experimental findings also enable a comparison with the strength predictions obtained from analytical models which are commonly used in the design of conventional reinforced concrete members. The discussions and comparative assessments presented in this paper provide an insight into the influence of various shear transfer mechanisms including transverse reinforcement, compressive zones, residual tensile stresses, aggregate interlock, and dowel action, in addition to the interfacial bond between the steel profile and concrete. The activation and contribution of the key shear transfer mechanisms are assessed in light of the experimentally-monitored crack growth, path and pattern, as well as in comparison with widely-adopted analytical approaches. The results show that the contribution of each transfer mechanism is a function of the crack kinematics and corresponding level of applied load. Finally, modifications to existing analytical approaches for conventional reinforced concrete elements are proposed in order to provide a reliable evaluation of the ultimate shear capacity of such hybrid systems. The suggested expressions account for the influence of the shear-arms' characteristics on the ultimate shear strength, and offer a more realistic prediction of the behaviour in comparison with conventional reinforced concrete design provisions.

© 2015 Elsevier Ltd. All rights reserved.

1. Introduction

Situations in which reinforced concrete floor elements need to be combined with vertical steel members often arise in multi-storey buildings, either due to loading and performance constraints or as a result of practical and constructional considerations. However, the design of such 'hybrid reinforced concrete/steel members' often poses various uncertainties related to the direct applicability of codified rules which are typically developed and validated for conventional reinforced concrete or structural steel configurations.

Many previous studies have examined the performance of various forms of hybrid steel/concrete elements. For example, various investigations have been carried out on the performance of composite steel coupling beams connected to reinforced concrete wall elements [1–4], and on the behaviour of connections between steel beams and reinforced concrete columns [5–7]. Several recent studies have also examined the performance of flat slab-to-tubular steel or composite column connections [8–11] by means of embedded shear-arms. Nevertheless, there is a dearth of fundamental assessments on the shear transfer mechanisms and ultimate behaviour of hybrid reinforced concrete beam-to-steel column systems.

The presence of an embedded steel element within a reinforced concrete member creates a discontinuity within two distinct regions (i.e. composite and non-composite), and results in more complex behavioural characteristics than those occurring in conventional reinforced concrete members. A number of failure modes can occur within the two regions of the hybrid member, either in flexure or shear, with the latter involving more intricate inter-dependent behavioural mechanisms. In a recent numerical study by the authors [12], typical shear failure mechanisms involving diagonal tension or shear crushing that can occur in hybrid beams, were explored. As expected, early stages of behaviour are described by flexural cracking. When flexural failure is not

---

Nomenclature

Greek letters

θ, θ_{cr}	crack inclination
Δ	deflection
Δ_{dow}	dowel displacement
Δ_s	crack slip
ε_i	strain
η	stiffness ratio ($E_c I_c / E_v I_v$)
λ	shape of the compression block factor, load proportionality factor
λ_K	proportionality constant
λ_v	embedded length factor
μ	friction coefficient
ρ_k	ratio between volume of aggregates to concrete
ρ_l	flexural reinforcement ratio
ρ_v	composite reinforcement ratio
ρ_w	shear reinforcement ratio
σ_i	normal stress
σ_{pu}	compressive strength of cement matrix
$\tau_{b,i}$	bond stress
τ_i	tangential stress
ψ	rotation
v_i	shear stress

Lowercase latin letters

a	shear span
a_v	composite shear span
a_i	lever arm
a_w, a_s	contact areas (for aggregate interlock action)
b	concrete section width
c	depth of the compression zone
c_{nom}	concrete cover
d	effective depth
d_b	bar diameter
$d_{g,i}$	aggregate dimension
e'	eccentricity
f_c	concrete cylinder strength
f_{ct}	concrete tensile strength
$f_{y,i}$	yield strength of steel
$f_{t,i}$	ultimate strength steel
h	concrete section depth
$h_{c,v}$	column depth

h_v	depth of the shear-key
l_{dow}	dowel span
l_v	embedded length
$l_{x,cr}$	horizontal projection of the shear crack
r_s	clear half span (from column face)
s_w	spacing of transverse reinforcement
z_i	lever arm
w_i	crack width
w_{max}	maximum crack width
x,y,z	coordinates

Uppercase latin letters

$A_{s,i}$	reinforcement sectional area
A_w, A_s	contact areas (aggregate interlock action)
A_v	shearkey cross sectional area
E_i	modulus of elasticity
I_i	moment of inertia
L_s	moment span
L	length
N_i	axial force
M_i	bending moment
P_i	applied load
V_i	shear force

Subscripts

agg	aggregate interlock
ch	concrete compressive zone
b	bond
c	concrete
cr	crack
s	longitudinal steel
dow	dowel action
max	maximum
res	concrete residual stresses
sw,i; *sw*; *w*	transverse reinforcement
STM	values from detailed assessment
test	test values
u	ultimate
v	composite slip, shearkey

---

governing and high shear forces are mobilised in the section, diagonal cracking occurs. Shear failure takes place when stresses cannot be transferred through the crack interfaces and the member divides into two rigid bodies rotating along a fixed point located at the crack tip in the compression zone. Shear transfer can include contributions from several mechanisms including the concrete compressive zone, aggregate interlock, dowel action and transverse reinforcement [13–26], as well as the interfacial bond between the steel member and surrounding concrete [27–29]. The activation of each mechanism depends on the material strength, reinforcement details and member size.

Taylor [14,15] carried out investigations focusing on the distribution of shear stresses in the compression zone of reinforced concrete beams by monitoring the strains using a detailed arrangement of electrical strain gauges. The results showed that, before cracking, the shear stress distribution is nearly parabolic and the force carried by the compression zone increases slowly up to 20–40% of the total shear force until the beam approaches failure. It was reported that the tension zone of the beam can carry

up to 75% of the total shear force, with the transfer through aggregate interlock contributing up to 33–50% of the total shear and the dowel action in the range of 15–25%; the latter two mechanisms decrease significantly when stirrups are present. The results presented by Swamy and Andriopoulos [22] are also in agreement with the above, and showed that shear transferred through aggregate interlock decreases with the increase in load.

Several models have been proposed to estimate the contribution of aggregate interlock to the ultimate shear strength [e.g. 16,17,19,22,30]. The model proposed by Walraven and Reinhard [16] and Walraven [17] accounts for the physical behaviour of the interlocking crack faces and is based on a cumulative distribution function of the aggregates in the crack plane. Modified approaches incorporating other width-to-slip relationships have also been proposed by Ulaga [31] and Guidotti [32]. On the other hand, Dei Poli et al. [19] adopted an idealised crack model where the aggregate interlock contribution was assessed by assuming that the reinforced concrete beam behaves as a plane truss with shear and confinement stresses along the diagonal cracks. In

general, shear transfer through aggregate interlock is often examined together with dowel action since they are strongly linked. Based on experimental observations, statistical assessments were carried out to estimate the interdependency between aggregate interlock and dowel action [22]. It was shown that the shear carried by the interface depends on the amount of longitudinal reinforcement, transverse reinforcement (spacing, intersection with governing crack and longitudinal reinforcement), concrete strength and moment-to-shear ratio.

Various investigations were also carried out to assess the capacity of a dowel in shear. For example, based on experimental observations from tests involving ribbed bars, Dei Poli et al. [20] developed formulations based on the subgrade stiffness of the concrete embedment. Several other models assumed that the dowel action can be assessed using an analogy with a beam on elastic foundation [33,34]. At ultimate state however, other studies [e.g. 20,35] indicate that this assumption is inaccurate owing to the non-linear behaviour of steel reinforcement and concrete within the embedment region. The non-linear behaviour can be captured by relating dowel bending to deformation by means of limit analysis as investigated by Paulay and Loeber [18], Chana [23] and more recently by Campana et al. [26]. On the other hand, the transfer through the fracture process zone was assessed by several researchers using the theory on fracture mechanics [38]. The transfer of residual stresses through the cracked interfaces follows a non-linear post-peak curve that is defined by a stress-crack opening relationship, the maximum crack width and uni-axial tensile strength of concrete. It is also worth noting that the contribution of the shear transferred by friction at the steel profile-concrete in composite members could be significant, but it depends on the surface properties, embedded length, concrete strength, and concrete cover. Wium and Lebet [28] showed that the resistance is highly depended on the size of the embedded steel section.

This paper focuses on examining the fundamental shear transfer mechanisms in hybrid structural systems consisting of reinforced concrete beams connected to steel columns by means of embedded 'shear-arms' (or 'shear-keys') which are directly welded to the steel columns and fully embedded in the reinforced concrete beams. A full account of the results of a series of five large scale tests on hybrid reinforced concrete beam-to-steel column assemblages is given. The tests are part of a wider European collaborative project which aims at providing a unified design procedure for various hybrid steel/concrete structural configurations. Based on detailed measurements of crack growth and propagation at various load levels approaching failure, the contribution of each shear transfer mechanism to the ultimate shear strength is quantified. Using the experimental results and observations, the paper also assesses the adequacy of strength predictions obtained from analytical models which are adopted in the design of conventional reinforced concrete members, with emphasis on European and North American provisions. Finally, an analytical approach is proposed in order to predict the ultimate shear behaviour of hybrid members of the form investigated in this paper.

2. Experimental programme

2.1. Testing arrangement

The layout of the testing arrangement is shown schematically in Fig. 1a, whilst Fig. 1b provides a general view of the test set-up. The test rig was designed to enable realistic experimental assessment of the ultimate behaviour of the large-scale hybrid beam/column specimens up to failure. The rig consisted of a main loading frame, on which an actuator of 1000 kN capacity was mounted, and two
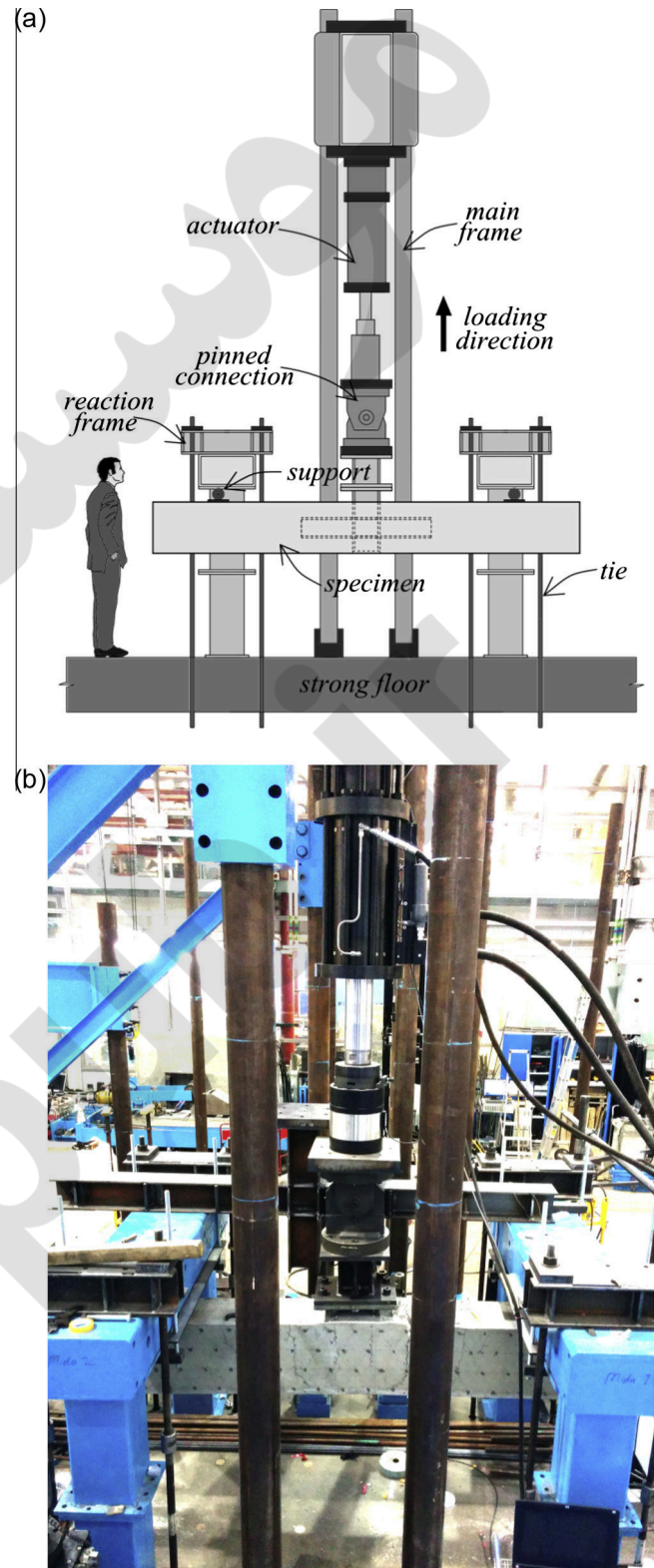

Fig. 1. Testing arrangement: (a) test-rig layout, (b) general view of test set-up.

reaction frames which provided the support points at both ends of the beam. Loading was applied by the actuator through a pinned connection at the top of the steel column section in the upward vertical direction, hence simulating vertical downward reaction loads at the two ends of the beam. The reactions between the specimen ends and the supporting frames were transferred through

two steel rollers of 100 mm diameter. Two steel plates 180 mm wide and 20 mm thick were positioned between the rollers and the specimen to avoid local effects at the supports. All tests were carried out in the displacement control mode of the actuator in order to enable detailed observation and measurement particularly at the ultimate stages of the response.

Besides the displacement and load measurements provided directly by the actuator, a number of independent displacement transducers were attached throughout the length of the specimen. In addition, detailed measurement of the initiation, growth and pattern of cracks was obtained by means of 'Demec' mechanical dial gauges. The Demec recordings were verified at several locations of the grid using a crack microscope. The crack pattern was captured by a digital camera at the load stages at which Demec measurements were taken. Strain gauges were additionally placed at various locations within the specimens. Procedures for monitoring crack development and strain gauge measurements are described in more detail in subsequent sections of this paper.

2.2. Specimen details

A series of five specimens were tested, and the main parameters varied were the embedded length of the shear-key (embedded length-to-steel member depth $l_v/h_v = 1.0$–3.6), the presence of transverse reinforcement (four specimens had stirrups with $\rho_w = 0.19\%$ and one without) and the stiffness ratio between the member and the shear-key; this ratio is represented by $\eta = E_c I_c / E_v I_v$ which is dependent on the elastic concrete modulus E_c assessed by means of the Eurocode 2 approach [39], the elastic moment of inertia of the concrete cross-section I_c, the elastic steel modulus E_v obtained from material tests and the moment of inertia of the shear-key I_v.

Fig. 2 shows a typical elevation (for half the tested element) and typical cross-sections for the specimens, whilst Table 1 summarises the details of the tested models. The dimensions of the specimens were selected based on practical ranges as well as experimental constraints, with the aim of achieving shear failure involving yielding of stirrups or concrete crushing. The specimens replicate the joint region of a hybrid frame structure that is made of steel columns and reinforced concrete beams. The joint region is represented by a steel column stub and two hybrid RC-composite cantilevers. The position of the supports depict the zero bending moment section of a continuous beam with moment span of about 6 m. A column section HEB240 was used in all five specimens. In four of the specimens (B25-R10-W20-S8, B10-R10-W20-S8, B36-R10-W20-S8 and B25-R10-W0-S8), HEB200 shear-keys were fully welded symmetrically on both sides of the column. The span used for these four members was $L_s = 2600$ mm. The fifth specimen (B25-R12-W20-S16) had a UC152 shear-key and a shorter moment span $L_s = 2300$ mm. The total length of all reported specimens was $L = 3750$ mm. The embedded length of the shear-keys l_v varied between 200 mm and 720 mm as indicated in Table 1.

The typical arrangement of longitudinal reinforcement consisted of $2\phi25$ bars crossing the steel column and $2\phi20$ bars positioned outside the column perimeter (Fig. 2b and c). The reinforcement ratio (ρ_l) was 1.09% for the first four specimens (i.e. B25-R10-W20-S8, B10-R10-W20-S8, B36-R10-W20-S8, and B25-R10-W0-S8) and 1.21% for B25-R12-W20-S16. Four $\phi12$ bars were placed at the bottom in all specimens to ensure continuity. The transverse reinforcement included equally-spaced two-legged stirrups of $\phi8$ mm. The spacing between the stirrups was $s_{w1} = 150$ mm within the moment span region and $s_{w2} = 70$ mm outside the moment span region. The actual effective depths of the specimens were determined by means of saw cuts throughout the depth of
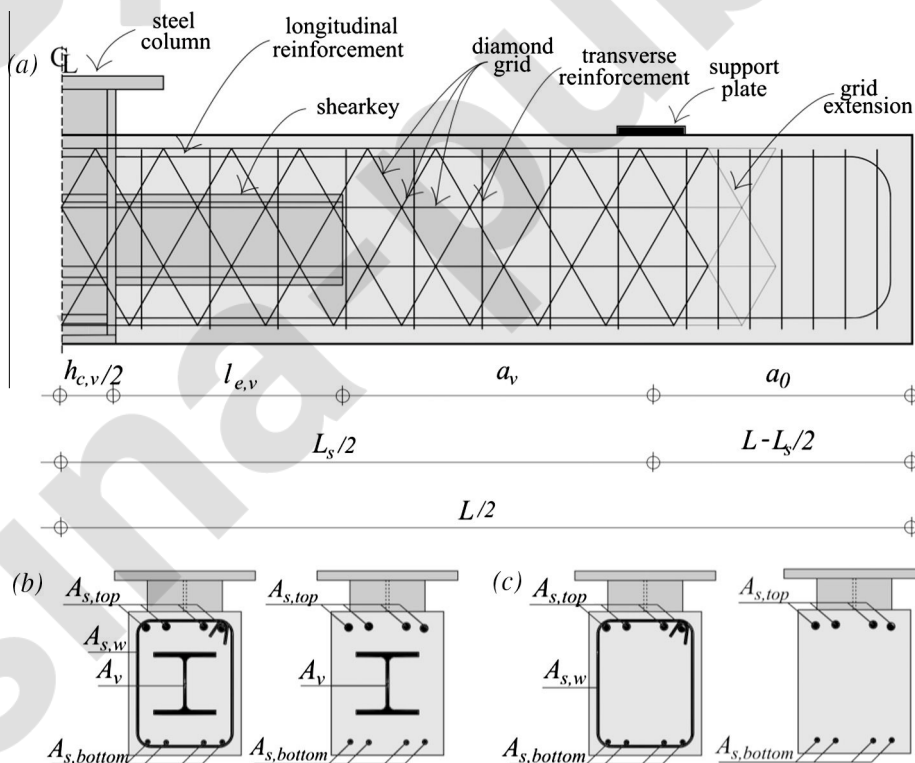

Fig. 2. Geometrical configuration, reinforcement layout and measurement system: (a) elevation view; cross sectional views within (b) composite and (c) non-composite sections for specimens with stirrups specimens without stirrups.

Table 1
Specimen details.

Specimen	Shearkey	RC cross section	l_v (mm)	L_s (mm)	d (mm)	ρ_l (%)	ρ_w (%)	f_c (MPa)	$f_{c,28d}$ (MPa)	Age (days)
B25-R10-W0-S8	HEB200	B360x455	500	2600	409	1.09	–	28.6	29.1	39
B10-R10-W20-S8	HEB200	B360x455	200	2600	412	1.09	0.19	27.3	29.1	28
B25-R10-W20-S8	HEB200	B360x460	500	2600	410	1.09	0.19	34.3	37.1	31
B36-R10-W20-S8	HEB200	B360x455	720	2600	408	1.10	0.19	29.9	29.1	35
B25-R12-W20-S16	UC152	B340x435	400	2300	391	1.21	0.20	28.7	29.1	50

Table 2
Steel properties.

Specimen	$f_{y0.2\%}$ (MPa)	$f_{t,i}$ (MPa)	ε_u (%)
HEB200 – flange	401	530	14.5
HEB200 – web	396	517	14.3
UC152 – flange	369	493	26.4
8 mm rebar	592	695	6.39
12 mm rebar	545	594	13.7
20 mm rebar	583	704	12.0
25 mm rebar	628	729	13.8

Notes: E_s = Elastic modulus, $f_{y0.2\%}$ = 0.2% proof stress, f_u = tensile strength and ε_u = the elongation after fracture;
Cross-sectional dimensions:
For HEB 200: $b \times t_f/d \times t_w/A_v$ = 200 mm $\times$ 15 mm/200 mm $\times$ 9 mm/7810 mm^2.
For UC152: $b \times t_f/d \times t_w/A_v$ = 154.4 mm $\times$ 11.5 mm/161.8 mm $\times$ 8 mm/4719 mm^2.

the specimens, and are given in Table 1. Material tests have been carried out in order to assess the strength and ductility characteristics of the steel used in the shear-keys and reinforcement bars. The average values of their properties based on a minimum three material tests are depicted in Table 2.

Ready mix concrete of Grade C25/30 with a maximum aggregate size of 10 mm was used in all specimens. A set of twelve samples were prepared to obtain the hardened concrete properties at 28 days and three samples to assess the strength on the day of testing. The samples used to determine the 28 day strength were immersed in water, whereas the others were maintained next to the test specimens. The compressive strength of concrete (f_c) obtained from cylinders on the day of testing varied from 27.3 to 34.3 MPa (Table 1), whilst the strength at 28 days ($f_{c,28d}$) varied from 29.9 to 38.7 MPa. The concrete compressive strength determined from cubes ($f_{c,cube}$) varied from 33.3 to 44.8 MPa, and the splitting tensile strength $f_{ct,sp}$ varied from 2.14 to 2.87 MPa.

2.3. Monitoring of cracks and strains

Detailed measurements of cracks were made at critical loading steps depending on the crack initiation, growth and pattern by means of a 'Demec' mechanical dial gauge. The Demec system incorporates a digital dial gauge and an Invar bar. A conical fixed point was mounted at one of the ends of the Invar bar and a pivoting point at the other end. The distance between the two conical points was 150 mm. In addition to strain gauges, strain measurements were also made by placing the two conical points in the holes within the steel discs which were attached to the concrete surface with adhesive. Each steel disc represented a relative measurement point. The number of Demec points varied from 74 to 82 representing a

'diamond' grid of 178 to 198 lines as indicated in Fig. 2. A purpose built program was developed in order to collect the data from the digital dial gauge via a COM PC port. Careful tracking of the recordings was followed in order to avoid the introduction of any spurious data. The first collection of data was performed at the initial configuration when the specimen was in the testing position (i.e. carrying only its own weight and the weight of the rollers). Table 3 presents the loading step when the Demec data collection was carried out, as discussed in more detail in subsequent parts of this paper. Each measurement was further processed to obtain the strain in various regions of the specimen. The instrumented load stages for each specimen, as a fraction of ultimate recorded load, were: 100% of $P_{u,test}$ for B25-R10-W0-S8, 83% of $P_{u,test}$ for B10-R10-W20-S8, 99% of $P_{u,test}$ for B25-R10-W20-S8, 90% of $P_{u,test}$ for B36-R10-W20-S8 and 94% of $P_{u,test}$ for B25-R12-W20-S16.

3. Experimental results and observations

3.1. Load–displacement response

The load (P_i) versus applied mid-span displacement (Δ) curves for all five specimens are shown in Fig. 3. On the other hand, Fig. 4 depicts a mapping of the crack pattern at failure. The specimen without transverse reinforcement B25-R10-W0-S8 showed the lowest capacity ($P_{u,test}$ = 350 kN). The three specimens with the same cross-sectional ratio (i.e. B360x455 and HEB200 shear-key) showed an increase in ultimate strength with the increase in embedded length. The specimen with the shortest shear-key, B10-R10-W20-S8, showed a peak load of $P_{u,test}$ = 647 kN. The reference specimen with intermediate embedment length, B25-R10-W20-S8, failed at $P_{u,test}$ = 710 kN, whereas in the case of that provided with the highest embedment length, B36-R10-W20-S8, the failure was recorded at $P_{u,test}$ = 788 kN. The strength of the fifth specimen reported herein, that had the same embedded length to depth ratio l_v/h_v but smaller concrete and shear-key cross-sections, failed at $P_{u,test}$ = 653 kN.

In the case of the specimen without shear reinforcement (B25-R10-W0-S8), flexural cracking was observed at about 24% of $P_{u,test}$. With increasing load, the struts forming between flexural cracks started to rotate and produced inclined cracking on the right-hand side of the specimen. Diminished propagation of cracking was observed on the opposite side. Failure occurred on the left-hand side due to the development of an inclined shear crack connecting the support and the tip of the column, and passing below the shear-key (Fig. 4a).

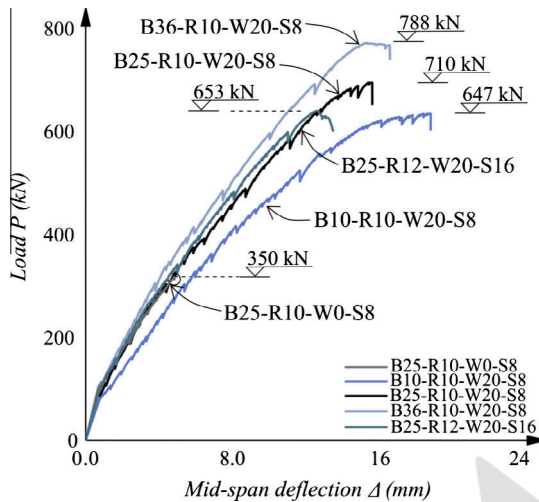The specimens provided with shear reinforcement (i.e. B10-R10-W20-S8, B25-R10-W20-S8, B36-R10-W20-S8,

Table 3
Test measurements.

Specimen	Shearkey	l_v/h_v (mm)	a_v/d (mm)	P_u (kN)	Δ_{Pu} (mm)	% P_u	V_{tot} (kN)	θ_{cr} ($^\circ$)	Failure mode
B25-R10-W0-S8	HEB200	2.5	1.44	350	5.50	100	175	40	S
B10-R10-W20-S8	HEB200	1.0	2.16	647	18.6	83	261	42	FS
B25-R10-W20-S8	HEB200	2.5	1.44	710	15.3	99	351	36	S
B36-R10-W20-S8	HEB200	3.6	0.91	788	15.2	90	356	44	S
B25-R12-W20-S16	UC152	2.5	1.38	653	12.5	94	353	37	S

Fig. 3. Load versus mid-span deflection response for the tested specimens.

B25-R12-W20-S16) exhibited similar behaviour throughout the loading process. The first flexural cracks were observed in the region of maximum bending moment at load levels around 10% of the ultimate load $P_{u,test}$. The flexural cracks had the tendency to form in the vicinity of transverse reinforcement at nearly uniform spacing. With increasing load, the flexural cracks located at the boundary between the reinforced concrete region and

composite region gradually rotated, intersecting the tip of the bottom flange of the shear-key.

In the case of the specimen with the shortest shear-key, B10-R10-W20-S8, the first diagonal crack was observed at about 40% of $P_{u,test}$ on the right hand side of the specimen. A diagonal crack with an inclination of 42° governed the behaviour up to load levels close to ultimate strength. The failure was characterized as mixed flexure-shear since high levels of strain were recorded in the longitudinal reinforcement (Figs. 4b and 5b). In the case of the Reference Specimen B25-R10-W20-S8, the first flexural cracks were recorded at about 7% of $P_{u,test}$ and inclined cracks propagated from the flexural ones at nearly 28.5% of $P_{u,test}$. Diagonal cracking due to direct formation of struts, developing from the edge of the support plate to the bottom tip of the shear-key, was observed at around 56% of $P_{u,test}$. Nearly symmetric cracks occurred on both sides of the specimen. The crack widths recorded during the test showed slightly larger values for the right hand side. However, failure occurred due to the development of a diagonal shear crack on the left-hand side of the specimen, starting from the support plate to the face of the column, joining a flexural crack and crossing below the bottom flange of the shear-key (see Figs. 4c and 5a). Failure was attributed to the yielding of the stirrups crossing the governing shear crack with an average inclination of 36°.

For the other extreme case, Specimen B36-R10-W20-S8 with the longest shear-key, diagonal cracking was recorded at 35% of $P_{u,test}$. The crack firstly developed from the tip of the shear-key towards the support at an inclination of 44°. The governing shear crack followed an elbow-shaped pattern developing below the
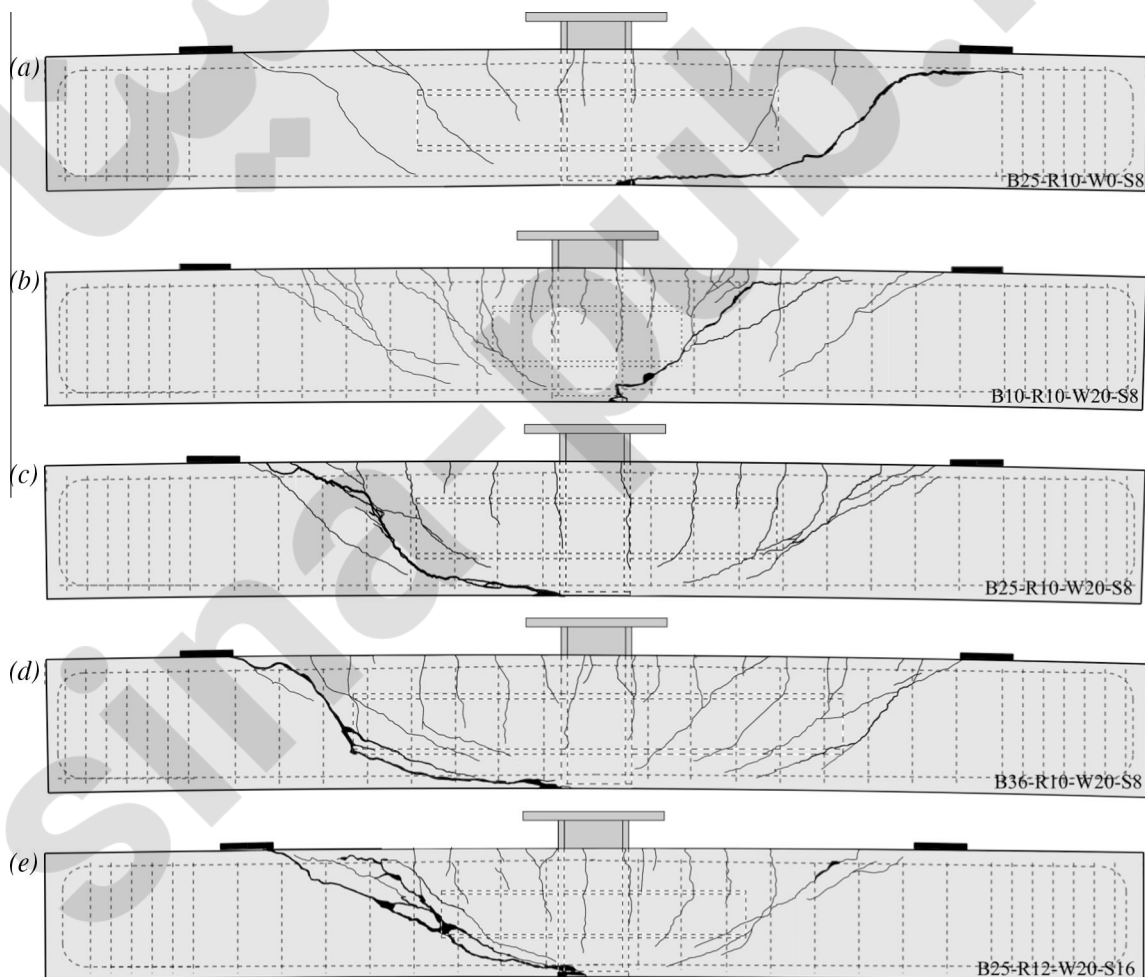

Fig. 4. Crack pattern at failure for the tested specimens: (a) B25-R10-W0-S8, (b) B10-R10-W20-S8, (c) B25-R10-W20-S8 (d) B36-R10-W20-S8 (e) B25-R12-W20-S16.
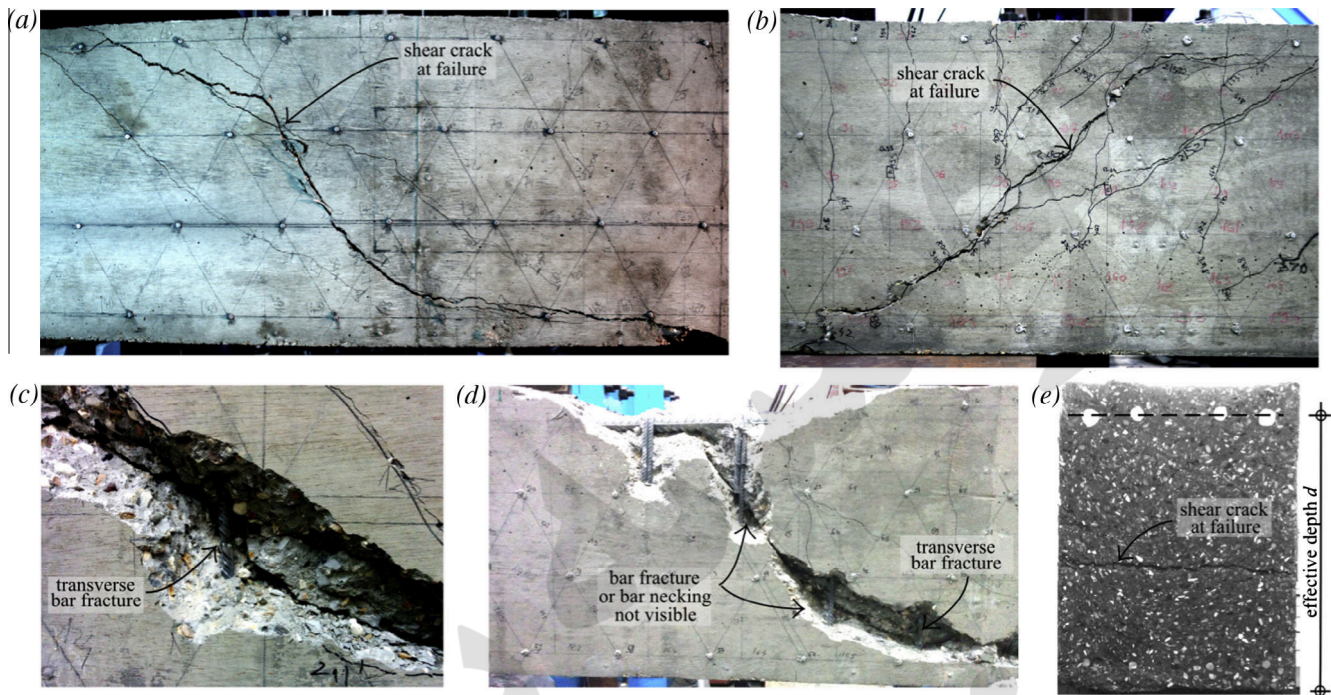
Fig. 5. (a) Governing shear crack in B25-R10-W20-S8. (b) Governing shear crack in B10-R10-W20-S8. (c) Transverse bar fracture. (d) Flexure-shear failure. (e) Saw-cut through specimen.

shear-key and reaching the steel column (Fig. 4d). On the right side of the specimen, parallel inclined cracks were observed at load levels between 278 and 649 kN in the shear-key region suggesting a composite action in shear. Failure attributed to shear initiated from the reinforced concrete section (outer region) between the support and tip of the shear-key. One stirrup fractured as observed after the removal of the concrete cover (Fig. 5d).

In the case of B25-R12-W20-S16, the first flexural cracks followed the line of the column flange and further growth was recorded with the increase in load. Diagonal cracks, firstly observed at 38%$P_{u,test}$, formed gradually in a relatively symmetrical pattern to the column axis on the monitored side of the beam. The governing shear crack developing at 37° commenced from the column edge in the compression zone, joining the tip of the shear-key. The final crack pattern was characterized by three cracks joining the root of the column to the support plate. Failure was attributed to the fracture of the nearest stirrup to the tip of the shear-key (Figs. 4e and 5c).

3.2. Shear transfer mechanisms

This section deals with the assessment of shear transfer mechanisms (STM) based on detailed test measurements using the mechanical dial gauges. As noted previously, and as described in Fig. 6, the crack width and crack slip were calculated accounting for the local crack inclination and the geometry of the grid. The direct result of using the 'Demec' mechanical gauge system is that accurate results regarding the development of the compression and tension stress fields in one-way specimens can be obtained. For example, this is illustrated in Fig. 7 which depicts a qualitative distribution of stress fields across the monitored face of the Reference Specimen B25-R10-W20-S8 at three loading stages. The geometry of the stress fields changes in agreement with the crack path and growth, showing an exact match between the crack path captured by the digital camera and stress fields by means of Demec measurements (Fig. 4c and plot corresponding to *0.99P_u* in Fig. 7). With the aid of the detailed test measurements, the

following sub-sections offer an assessment of aggregate interlock, dowel action, shear carried by the compressive zone, contribution of transverse reinforcement, composite slip between the steel shear-key and the concrete free body, as well as the transfer mobilised through the fracture process zone. The Demec measurements, used to determine the contribution of each shear transfer mechanism, were taken at the following loading stages: 100% of $P_{u,test}$ for B25-R10-W0-S8, 83% of $P_{u,test}$ for B10-R10-W20-S8, 99% of $P_{u,test}$ for B25-R10-W20-S8, 90% of $P_{u,test}$ for B36-R10-W20-S8 and 94% of $P_{u,test}$ for B25-R12-W20-S16.

3.2.1. Aggregate interlock

As illustrated in Fig. 8a, as the crack width and slip increase, the edges of the aggregates protrude to the opposite face of the crack resulting in plastic deformations in the cement paste which, for normal strength concrete, has lower strength than the aggregates (Fig. 8b) [16,17]. The aggregate interlock contribution is dependent on the roughness of the crack interface, aggregate type, their embedment depth in the cement paste, the magnitude of the slip, and the opening of the two interfaces. In the current investigation, the model developed by Walraven [16,17] is employed (Fig. 8a).

Accounting for the embedment of the aggregate in the cement paste, the model considers the following contact phases between the aggregate particle and the cement matrix: growing contact phase, maximum contact phase and no contact. The shear and normal stresses acting on the crack interface are defined by the following:

$$\sigma_{agg} = \sigma_{pu}(A_s - \mu \cdot A_w) \tag{1a}$$

$$\tau_{agg} = \sigma_{pu}(A_w + \mu \cdot A_s) \tag{1b}$$

The contact areas A_s and A_w depend on the crack width w, crack slip Δ_s, the maximum aggregate diameter d_g and the total aggregate volume per unit volume of the concrete ρ_k. The matrix compressive strength σ_{pu} is related to the concrete compressive strength and the coefficient of friction $\mu = 0.5$ (Fig. 8b), as follows:
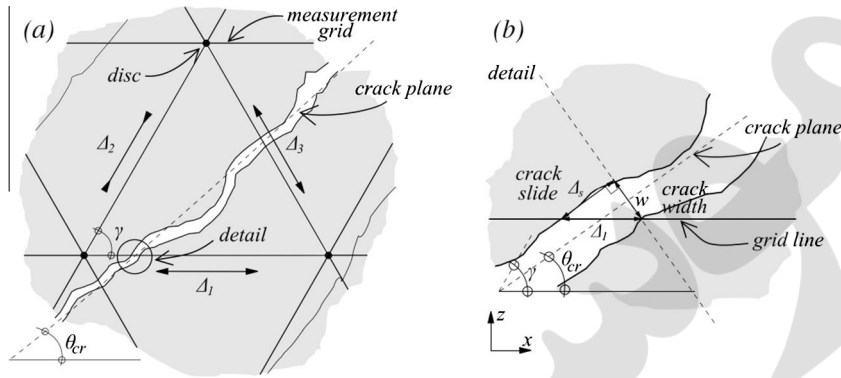
$$\sigma_{pu} = 5.83 f_c^{0.63} \tag{2}$$

Fig. 6. (a) Detail of the Demec measurement grid and intersecting shear crack. (b) Detail of shear crack width w and slip Δ_s assessed from recorded horizontal displacement Δ_1.

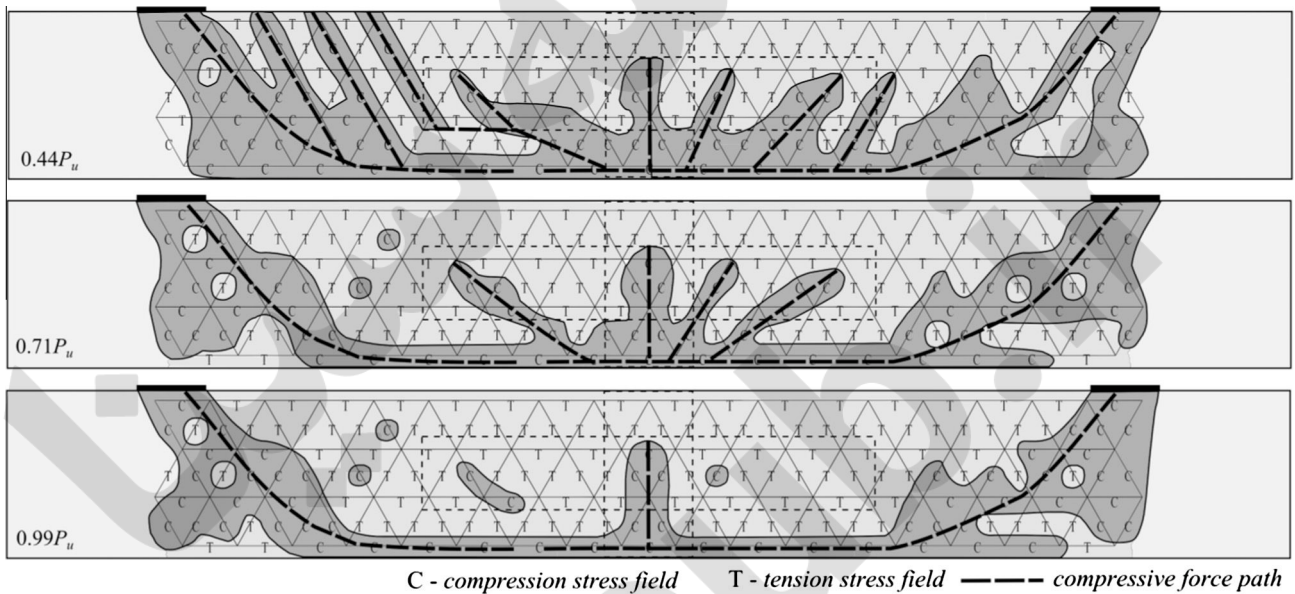C - *compression stress field*   T - *tension stress field*   ——— *compressive force path*

Fig. 7. Qualitative strain maps for Specimen B25-R10-W20-S8 at various loading stages.
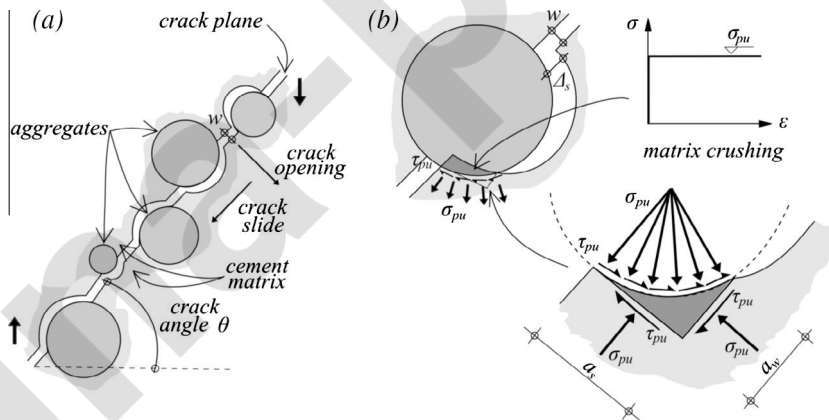

Fig. 8. (a) Aggregate interlock mechanism. (b) State of stresses in the cement paste due to the interlock with an aggregate particle and rigid plastic stress–strain diagram for cement matrix.

The general formulation, dependent on the contact phase (magnitude of crack slip and crack width) of the contact areas, is given by Eq. (3).

$$A_i = \int_{d_1}^{d_2} \rho_k \frac{4}{\pi} \cdot F\left(\frac{D}{d_g}\right) \cdot G_k(\Delta_s, w, D) \cdot dD (i = w, s) \tag{3}$$

The simplified model in [16,17] accounts for maximum aggregate dimensions between 16 and 32 mm. In the current study, concrete with a maximum aggregate dimension $d_{g,max}$ = 10 mm is used, therefore Eq. (3) was employed to obtain the contact areas A_w and A_s. It can be observed that the contact areas A_w and A_s, and consequently the interfacial stresses, decrease with the

increase of crack width and slip. On the other hand, the maximum dimension of the aggregate has a significant influence on the analytical prediction for large crack widths and crack slip. For the extreme cases ($w = 1.0$ mm; $\Delta_s = 2.0$ mm), the contact areas for $d_g = 10$ mm is about half that in the case of $d_g = 32$ mm (Fig. 9a).

The contribution of this shear transfer mechanism was accounted for using an average distribution of stresses over the governing shear crack at the instrumented loading stage (Fig. 9c). The normal and tangential stresses acting on the crack interface are based on the detailed local recordings. It can be seen that for loading stages close to ultimate strength, the crack widths and slips show larger values, therefore the contribution is modest (e.g. 6% of the estimated shear transfer at 99% $V_{u,test}$ for B25-R10-W20-S8). On the other hand, at early loading stages the contribution is significant (e.g. 28% of the total shear transfer at 83% of $V_{u,test}$ for B10-R10-W20-S8) (Table 4). The contribution of this mechanism reduces as the specimen reaches the ultimate limit state. In specimens without shear reinforcement, narrower crack widths are expected, therefore the contribution becomes significant (e.g. 32% of the determined shear transfer at failure for B25-R10-W0-S8).

3.2.2. Dowel action

One of the main instigators for shear failures in beams without transverse reinforcement is the cracking initiation and splitting of concrete at the level of the longitudinal reinforcement bars [24]. In cases with large stirrup spacing, similar behaviour occurs as well. When transverse reinforcement is present, failure develops in a more controlled fashion; splitting is blocked and the beam remains stable up to the yielding of the stirrups or yielding of flexural reinforcement. Activation of dowel action requires a level of dowel displacement Δ_{dow} involving a combined set of effects in the crack region, such as bending of the dowel as well as secondary effects (concrete breakout and concrete spalling at ultimate limit state) (Fig. 10a). The dowel force depends on the diameter of the bar,

layout of the tension bars, width of the dowel failure surface and the concrete tensile strength. The relationship between dowel bending and dowel displacement can be determined by means of limit analysis. Dowel bending occurs as a consequence of the application of two concentrated forces separated by the dowel span l_{dow} (Fig. 10b). Accounting for the moment equilibrium at the centre-line of the dowel span and for the level of stress in the dowel bar, the ultimate dowel force (as result of formation of two plastic hinges) is given by Eq. (4). Dowel bending takes place as the load increases. Concrete breakout occurs for thick concrete covers, typified by the dislocation of small cones under the reinforcement bars, whereas spalling occurs for thin concrete covers. The contribution of these two mechanisms depends on the tensile stresses in the concrete in the vicinity of the dowel (Fig. 10a). It can be shown that the shape of the breakout cone is mainly attributed to the dowel diameter. The depth of the cone (radius) is about $0.5d_b$ and the height is $1.5d_b$ (Fig. 10c [20]). The required force to produce concrete breakout can be approximated by Eq. (5), and the force leading to spalling by Eq. (6). The total contribution of the dowel action at ultimate state is predicted by the sum of the primary and secondary mechanisms related to the dowel bending as given by Eq. (7).

$$V_{dow,u} = \frac{d_b^3 \cdot f_{ys} \left(1 - \frac{\sigma_s}{f_{ys}}\right) \cdot \cos\left(\frac{l_{dow}}{\Delta_{dow}}\right)}{3 \cdot l_{dow}} \tag{4}$$

$$V_{dow,br} = \frac{\pi}{4} d_b^2 (0.5 + \sqrt{2.75}) f_{ct} \tag{5}$$

$$V_{dow,sp} = c_1 \cot\theta \cdot f_{ct} \tag{6}$$

$$V_{dow} = V_{dow,u} + V_{dow,br} + V_{dow,sp} \tag{7}$$

Fig. 10d plots the relationship between the dowel span l_{dow} and the dowel action V_{dow} accounting for the flexural reinforcement existing in the test specimens (i.e. $2 \times \phi 25 + 2 \times \phi 20$). The
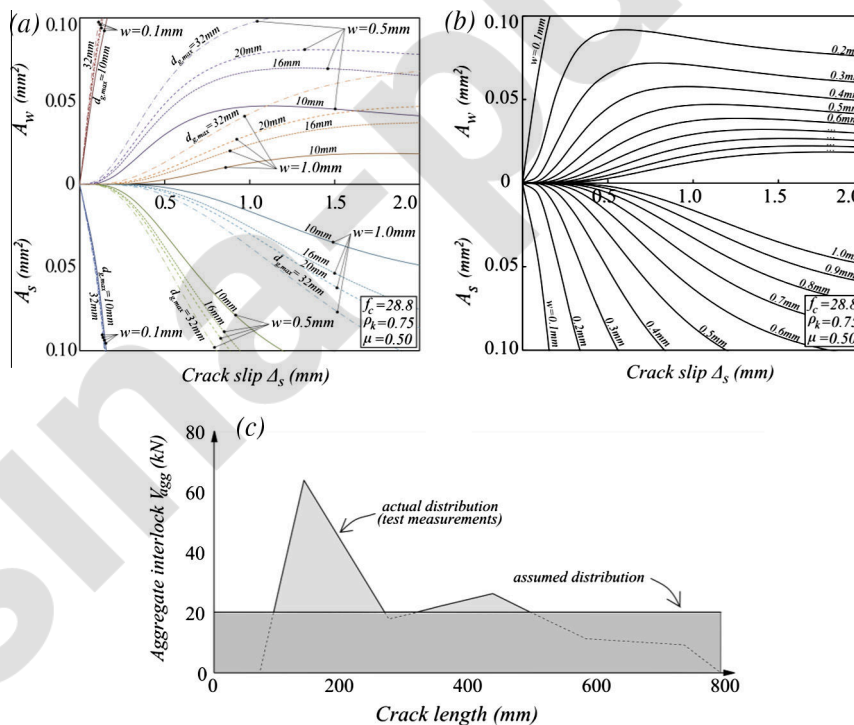

Fig. 9. Contact areas according to Walraven [16,17]: (a) influence of aggregate size on the contact areas, (b) influence of crack width and shear displacement over the contact areas for $d_{g,max} = 10$ mm, (c) aggregate interlock distribution according to test measurements and assumed one for B25-R10-W20-S8.

Table 4
Shear transfer mechanisms assessment results.

		Aggregate interlock	Dowel action	Composite slip	Shear reinforcement				Compressive zone	ΣV_i (kN)	$V_{u,test}$ (kN)	$\Sigma V_i/V_{u,test}$
					V_{sw1}	V_{sw2}	V_{sw3}	V_{sw4}				
B25-R10-W20-S8	V_i (kN)	20.1	0.27	21.9	59.5	59.4	59.5	37.2	83.8	342	351	0.97
	N_i (kN)	18.5	977	27.4	–	–	–	–	583			
	x_i (mm)	708	935	633	486	640	795	943	232			
	y_i (mm)	205	392	133	–	–	–	–	35			
B10-R10-W20-S8	V_i (kN)	72.3	2.56	7.78	25.3	6.55	–	–	107	225	267	0.84
	N_i (kN)	81.4	827	9.72	–	–	–	–	669			
	x_i (mm)	404	594	303	349	498	–	–	232			
	y_i (mm)	265	411	151	–	–	–	–	32.5			
B36-R10-W20-S8	V_i (kN)	75.2	12.1	53.3	59.6	29.9	–	–	103	337	356	0.95
	N_i (kN)	48.7	824	63.2	–	–	–	–	447			
	x_i (mm)	786	970	685	695	845	–	–	706			
	y_i (mm)	222	408	159	–	–	–	–	41.5			
B25-R10-W0-S8	V_i (kN)	49.0	71.6*	–	–	–	–	–	30.9	152	175	0.87
	N_i (kN)	57.7	363	–	–	–	–	–	187			
	x_i (mm)	882	1000	–	–	–	–	–	676			
	y_i (mm)	205	414	–	–	–	–	–	42.3			
B25-R12-W20-S16	V_i (kN)	56.7	12.6	11.6	35.8	40.7	59.7	39.2	44.3	305	326	0.93
	N_i (kN)	38.2	786	7.22	–	–	–	–	578			
	x_i (mm)	474	770	444	198	4321	467	611	196			
	y_i (mm)	282	397	133	–	–	–	–	27.5			

* Accounts for the secondary transfer mechanisms (at $1.00V_u$).

contribution of the dowel action to the shear transfer is significant for small dowel spans. As the dowel span increases, the dowel action diminishes (e.g. the case of B10-R10-W20-S8 where l_{dow} = 616 mm). Accounting for Eq. (4), the magnitude of the dowel action is dependent on the dowel stress. For stress levels approaching the yield strength, the dowel action tends to be non-existent (e.g. the case of B25-R10-W20-S8, where σ_s/f_{ys} = 0.99). All specimens provided with transverse reinforcement showed stress levels in the longitudinal reinforcement higher than 80% of its yield strength. Consequently, in such configuration, the dowel action becomes rather insignificant with respect to the total shear transfer. The secondary mechanisms are not accounted for in the shear transfer for these members since they are only activated at ultimate state, and the measurements were taken prior to that point. However, in the case of B25-R10-W0-S8, the stress in the reinforcement was σ_s/f_{ys} = 0.31, the dowel span l_{dow} = 177 mm, and the measurements were taken at failure (at 350 kN, whereas the ultimate strength based on the load recorded by the load cell was $P_{u,B25-R10-W0-S8}$ = 350.06 kN); the contribution is therefore high as it accounts for primary (dowel bending) and secondary (concrete breakout and spalling) mechanisms – as indicated in Table 4.

3.2.3. Concrete compressive zone

The shear carried by the concrete compressive zone is dependent on the member size, neutral axis position and internal force distributions. The compressive strength of concrete affects the state of stresses and shear strength. The current investigation assesses the transfer through the concrete compressive zone by considering a series of internal equilibrium equations on the free body diagram in Fig. 11. The forces involved in the shear transfer V_{tot} are the transfer through the compressive zone V_{ch}, dowel action V_{dow}, aggregate interlock V_{agg}, concrete residual stresses V_{res}, composite slip V_v and transverse bars intersected by the governing shear crack $\Sigma V_{sw,i}$ (Eq. (8)).

$$V_{tot} = V_{ch} + V_{dow} + V_{agg} + V_{res} + V_v + \Sigma V_{sw,i} \tag{8}$$

Accounting for the moment equilibrium about the rigid body rotation point (Figs. 11 and 12):

$$\Sigma(V_{sw,i}a_{sw,i}) + V_{dow}a_{dow} + V_{agg}a_{dow} + V_{res}a_{res} + V_v a_v$$
$$+ N_{ch}(d - 0.5\lambda c) - V_{tot}a_i = 0 \tag{9}$$

The shear stresses in the compression zone are in the form of a parabola at early loading stages (elastic stage – $v_{ch,max}$ at the neutral axis), whereas at stages near ultimate, the maximum shear stress $v_{ch,max}$ is found to be above the neutral axis in the compressive block [15]. For simplicity, the current study accounts for a uniform distribution of shear and normal stresses in the concrete compression zone (Fig. 13), as follows:

$$v_{ch} = \frac{V_{ch}}{b \cdot \lambda c} \tag{10a}$$

and

$$\sigma_{ch} = \frac{N_{ch}}{b \cdot \lambda c} \tag{10b}$$

Under the applied load P_i, the shear stresses and the normal stresses in the shear critical zone increase proportionally. Consequently, they can be related to a proportionality constant λ_K [36,37] as follows:

$$\sigma_{ch} = \lambda_K \cdot v_{ch} \tag{11a}$$

where $\lambda_K = l_{x,cr}/c \tag{11b}$

in which $l_{x,cr}$ is the length of the horizontal projection of the diagonal shear crack.

The horizontal projection of the shear crack results from the recorded crack pattern at the instrumented loading stage. On the other hand, the depth of the compression zone is estimated with due account for the linear distribution of strains between the tension and compression zones, using the test measurements based on the Demec grid and visual observations at the corresponding loading stage.

For Specimen B10-R10-W20-S8, the depth of the compression zone was estimated as 65 mm corresponding to an applied load P_i = 535 kN. Limited flexural cracking was observed in the shear span, hence the inclined compressive stress field was not disturbed
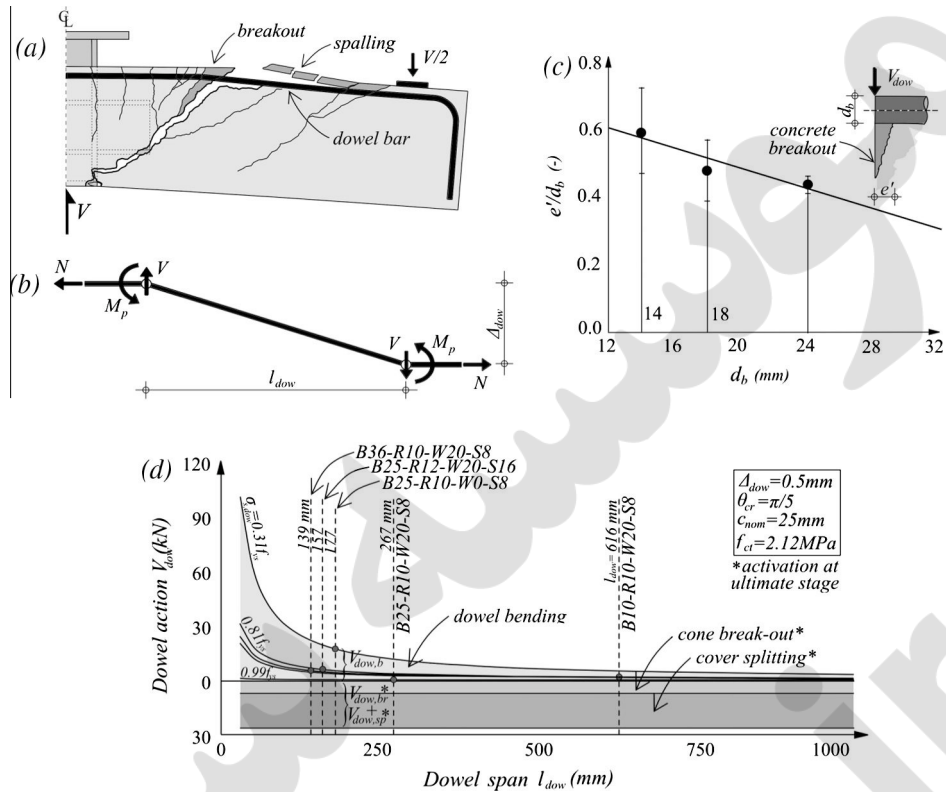
Fig. 10. Dowel action: (a) Mechanisms involved. (b) Limit analysis. (c) Dimensions of the breakout cone according to Dei Poli et al. [20]. (d) Contribution of dowel bending and potential secondary mechanisms to the dowel action.
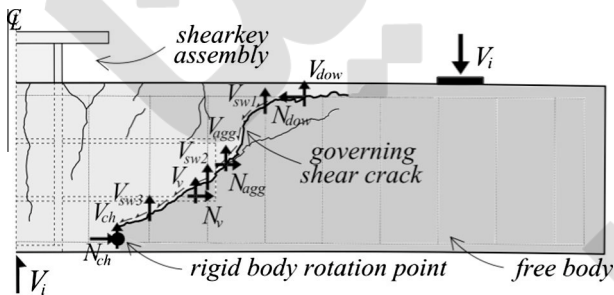

Fig. 11. Free body diagram (general case).

– maintaining its elastic configuration throughout nearly the entire loading process. The contribution of shear transfer via the concrete compression zone to the total shear is significant (up to 41% of the shear force). The Reference Specimen B25-R10-W20-S8 showed a similar behaviour. The depth of the compression zone was found to be $c = 70$ mm at 99% of the ultimate strength. Due to the large contribution of the stirrups, accounting for the equilibrium conditions indicates that 24% of the shear is transferred through the compressive zone. The specimen with the longest shear-key (B36-R10-W20-S8) shows a reduced transfer through the compressive zone (29% of the estimated shear force for $c = 83$ mm) at 90% of the ultimate strength. For tests where the measurements were taken near the ultimate limit state, the contribution reduces considerably since the neutral axis drops to very low values and shear is predominantly carried by stirrups.

3.2.4. Transverse reinforcement

The total amount of shear force carried by the transverse reinforcement is determined by the level of stress, bar diameter and bond characteristics. Reinforcement forces were calculated according to bar diameter and rebar stresses. Demec measurements were converted into strains by considering the 150 mm Demec gauge length and local crack inclinations. Accounting for material properties as reported in Table 2, the reinforcement stress was determined assuming bi-linear constitutive laws.

The strain in a transverse bar is given by the strain resulting from the governing shear crack intersecting the bar. In the tests presented herein, the stirrups were intersected by a number of inclined cracks besides the governing one (Fig. 14a). The peak strain in the stirrup $\varepsilon_{sw,i}$, as predicted by Eq. (12), is given by the width of the governing shear crack w_{cr} intersecting the stirrup (accounting for its inclination; with reference to the maximum crack widths plotted in Fig. 12 for each specimen at the instrumented load stage). The cracking strain is subtracted in the calculations ($\varepsilon_{ct,cr} = f_{ct}/E_c$) from the direct test recordings.

$$\varepsilon_{sw,i} = \frac{w_{cr}}{l_{sw,i}} \tag{12}$$

The contribution of one transverse bar is given by:

$$V_{sw,i} = \frac{\pi}{4} d_b^2 E_{sw} \varepsilon_{sw,i} \tag{13}$$

The specimens in this study were reinforced with closed stirrups with each branch of $d_{bw} = 8$ mm ($A_{sw,i} = 2\phi 8$ mm) spaced at $s_w = 150$ mm. The material properties of the stirrup steel materials are reported in Table 2. The post-yield modulus considered for the hardening branch of the bilinear stress–strain diagram used in the investigations is $E_{shw} = 1518$ MPa (Fig. 14b). Accounting for the total length of the stirrup $l_{sw} = 402$ mm, the average crack width at yielding of the two branches of one stirrup is $w \approx 2.4$ mm.

The contribution of the transverse reinforcement is dependent on the crack kinematics (pattern and width). The inclination of the shear crack (Table 3) is one of the governing parameters: a
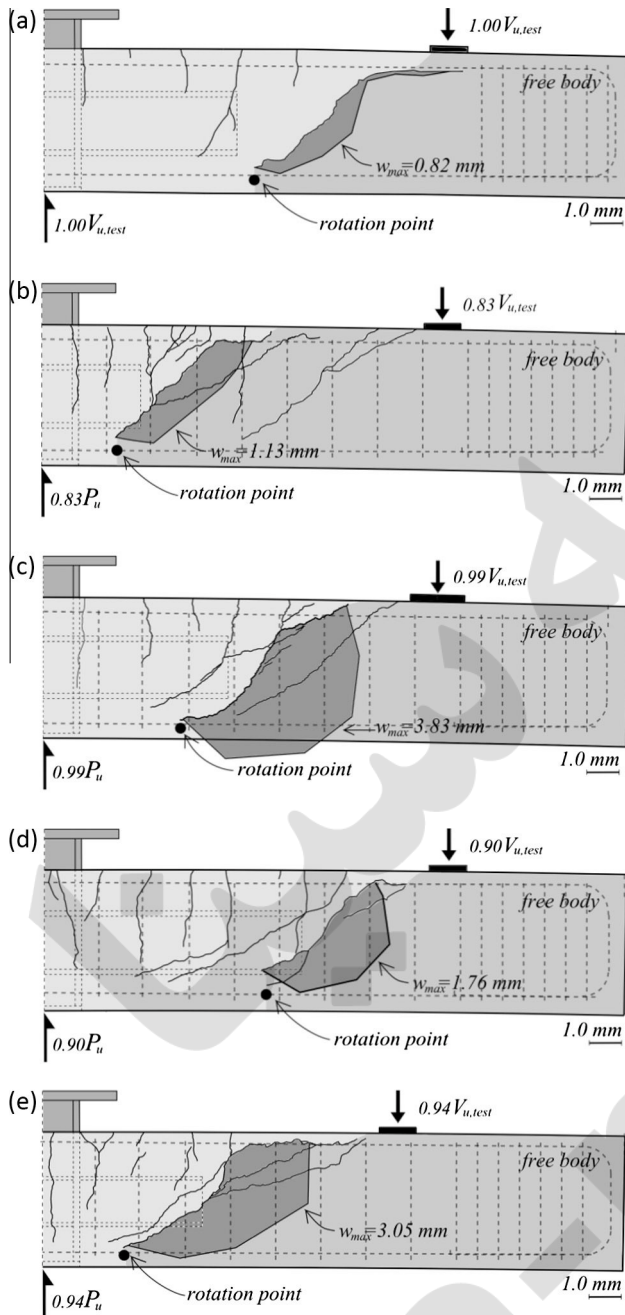
Fig. 12. Free bodies and maximum crack width at the instrumented load step of the tested specimens: (a) B25-R10-W0-S8. (b) B10-R10-W20-S8. (c) B25-R10-W20-S8. (d) B36-R10-W20-S8. (e) B25-R12-W20-S16.

steeper crack intersects a reduced number of stirrups (2 stirrups in case of B10-R10-W20-S8 and B36-R10-W20-S8), whereas the presence of a flatter crack results in the activation of an increased number of stirrups (4 stirrups for B25-R10-W20-S8 and B25-R12-W20-S16). Therefore, the contribution of stirrups to the total shear transfer is high for B25-R10-W20-S8 and B25-R12-W20-S16 (61% and 53%, respectively) and relatively lower for B10-R10-W20-S8 and B36-R10-W20-S8 (12% and 25%, respectively), as indicated in Table 4.

3.2.5. Shear-key contribution

In the elastic and flexural cracking stages, the bottom flange of the shear-key acts as support for the governing strut. In case of isolated specimens, as those reported in this paper, the embedment

length influences the specimen behaviour in the sense that the strut inclination depends on the composite shear span (i.e. the distance between shear-key tip to the support). In case of long embedment lengths, direct transfer in the composite span is likely to occur. On the other hand, in case of short shear-key, the direct transfer reduces as the composite shear span increases. An increase in loading leads to higher stress in the strut and eventually to the development of a diagonal crack below it. In some cases, the governing shear crack intersects the shear-key just below the inclined strut (Specimens B10-R10-W20-S8, B36-R10-W20-S8, B25-R12-W20-S16). At ultimate state, the rigid body rotation axis drops below the bottom flange of the shear-key. As a result of the rotation, the body slips from the shear-key (Fig. 15a). The amount of force necessary to produce the slip is directly related to the shear crack width. After slip occurs, a residual amount of bond exists between the two interfaces (a typical bond-slip relationship is depicted in Fig. 15b).

The influence of the cross-sectional size of the shear-key was investigated by modifying the stiffness ratio η as explained in Section 2.2. The section size varied from HEB200 for Specimen B25-R10-W20-S8 to UC152 for Specimen B25-R12-W20-S16. For both specimens, the embedment length-to-shear-key depth ratio ($l_v/h_v = 2.5$) and moment span-to-effective depth ratio (L_s/d) were maintained constant. Both the flexural and shear reinforcement ratios were similar (refer to Table 1). As depicted in Fig. 3, the stiffness response of the two specimens is similar, whereas the ultimate strengths differ by 8%. Both specimens showed similar response up to ultimate, failing in shear. At the instrumented load stage (99% of P_u for specimen with HEB200 and 94% of P_u for specimen with UC152 shear-key), the governing shear crack intersected four stirrups with at least one stirrup yielding. The strain levels in the shear-key flange were in the elastic regime. At ultimate, the peak strain, located in the vicinity of the steel column, reached values of 37% of the yield strain for the specimen with HEB200 shear-key and 75% of the yield strain for the specimen with UC152 shear-key. Despite the fact that the flexibility of the shear-key was not investigated here, it is likely that for low stiffness ratios η (i.e. small shear-key section size-to-beam cross-section), inelastic behaviour of the shear-key could govern the behaviour leading to a more flexible beam response than the one observed in the current test programme.

Based on the experimental database reported by Roeder et al. [29] (Fig. 15c), the maximum bond stress accounted for in practice is smaller than the measured range. In the current study, a lower bound of the maximum bond stress is accounted for in Eq. (15); a value consistent with the published results [28] for HEB200 profiles embedded in concrete was adopted. A simple Coulomb criterion is applied to estimate the frictional resistance of the shear-key against the concrete body. Accounting for a linear interaction between the frictional resistance and slip (crack width) for a smooth steel interface embedded into a concrete body, the shear transfer owing to the composite action between the shear-key and concrete is given by Eq. (14). The friction coefficient accounted for in this study is $\mu = 0.8$ according to values reported in previous studies [27,28].

$$V_v = 2\mu \cdot \tau_{b,v} \cdot b_v c_v \cdot \cot\theta \tag{14}$$

$$\tau_{b,v,\max} = 0.5 \text{ MPa} \tag{15}$$

$$\Delta_v(\tau_{b,v,\max}) = 0.1 \text{ mm} \tag{16}$$

The shear-friction contribution between the concrete free body and the shear-key is determined by accounting for the total slip across the inclined cracks intersecting the flanges of the shear-key for Specimens B25-R10-W20-S8, B10-R10-W20-S8, B25-R10-W0-S8 and B25-R12-W20-S16. This mechanism was not
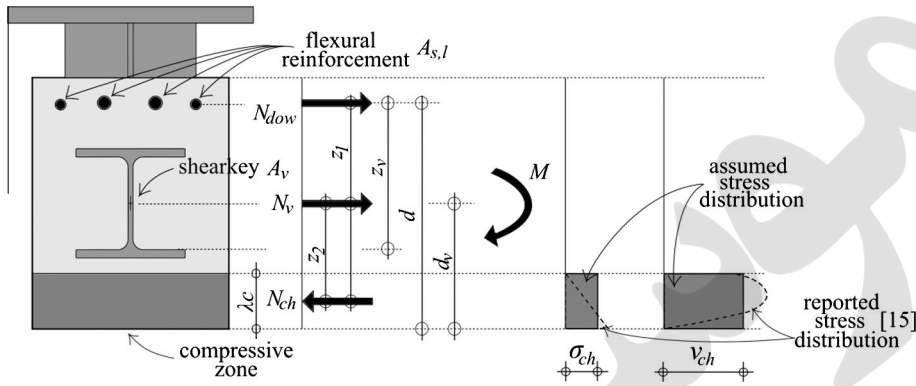
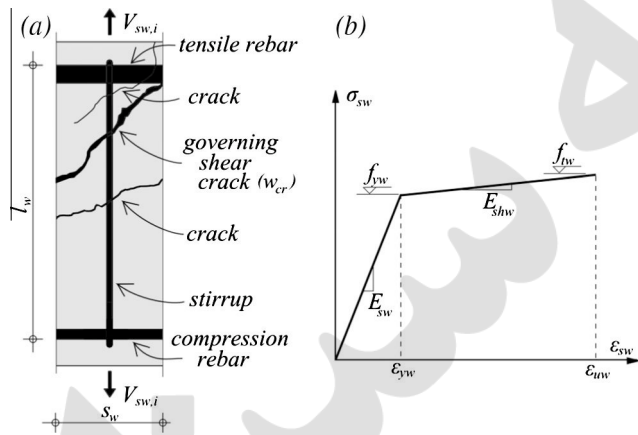**Fig. 13.** Assumed stress distribution in the compressive zone.

Fig. 14. (a) Stirrup subjected to traction as a consequence of crack opening. (b) Bi-linear stress–strain relationship for steel.

accounted for in Specimen B25-R10-W0-S8 since no inclined crack intersected the shear-key (Fig. 12d). Considering Eq. (14), the contribution of the 'composite slip' mechanism varies from 3% to 15% of the total shear force.

3.2.6. Concrete residual stresses

Shear cracks extend when the concrete is unable to transfer elastic stresses at the crack tip ($\sigma_{ct} \geqslant f_{ct}$). Even if the concrete tensile strength is attained, stresses can be transferred through the fracture process zone as long as the corresponding crack width is small. According to fracture mechanics concepts [38], the crack propagation in concrete is modelled by a fictitious crack defined by a region where aggregate interlock is activated and a true traction-free crack in a unique crack plane.

4. Comparative assessments

4.1. Contribution of shear transfer mechanisms

Evaluation of the detailed experimental results, in the above sections, provided in-depth insights into the contribution of
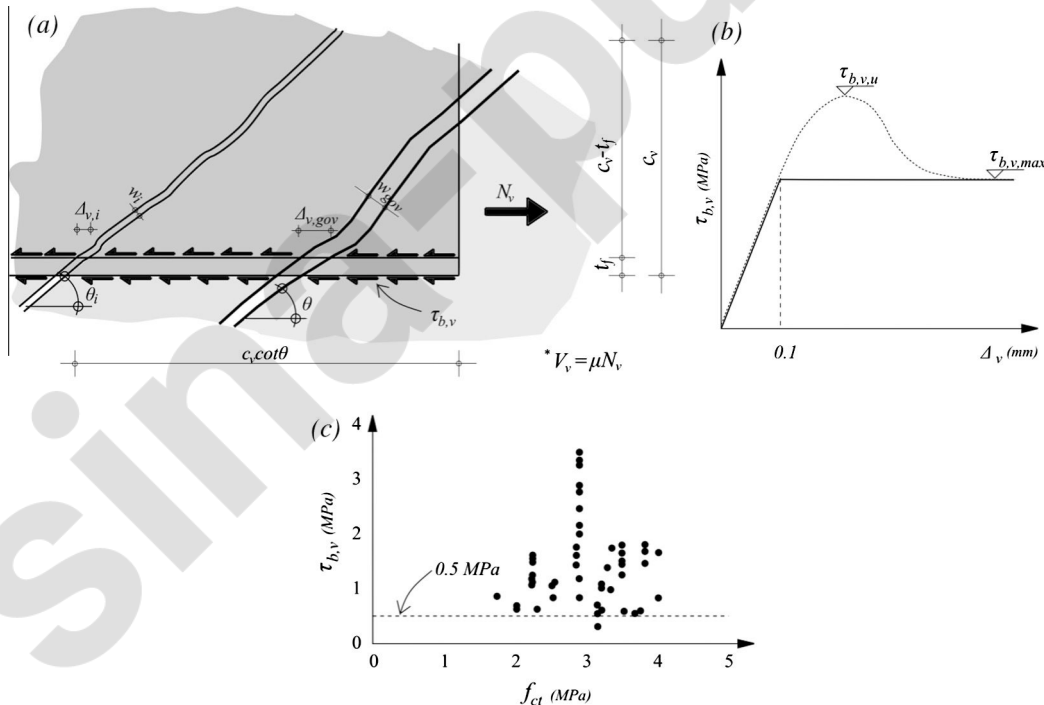

Fig. 15. (a) Contribution of the friction resistance between shear-key and concrete body to total shear. (b) Bi-linear bond-slip relationship for smooth interfaces embedded in concrete subjected to traction. (c) Relationship between concrete tensile strength and maximum average bond stress – adapted from the database reported by Roeder [29].

different shear transfer mechanisms. The contribution of each mechanism, as summarised in Fig. 16 for the five large-scale specimens, varies according to the crack pattern and kinematics and also with the magnitude of applied load. The crack pattern and kinematics are clearly influenced by the presence of stirrups, amount of flexural reinforcement and length of the shear-key. The presence of a steel insert in the RC section alters the shear behaviour (in comparison with a typical RC member), largely by reducing the shear span and increasing the direct strutting action.

As the transferred force increases, the dowel forces acting at the crack produce bending of the tension reinforcement causing separation of the concrete cover from the dowel (at ultimate state). Due to the increase in stress in the inclined strut, the perpendicular strain exceeds the cracking strain of concrete. As a result, the diagonal crack grows further towards the compression zone causing instantaneous failure in beams without shear reinforcement (i.e. in Specimen B25-R10-W0-S8). When transverse reinforcement is provided, failure takes place in a controlled fashion. The stirrups carry the load up to yield (e.g. in Specimens B25-R10-W20-S8 and B25-R12-W20-S16). At early loading stages (e.g. serviceability state) a higher shear is transferred by the compressive zone since the neutral axis is closer to the median axis. In the case of Specimen B10-R10-W20-S8, the compressive zone carries 41% of the shear at 83% of the ultimate strength $V_{u,test}$. In the case of other specimens, the contribution of this mechanism decreases substantially up to 14% for B25-R12-W20-S16 at 94% of its ultimate strength.

Transverse reinforcement, when available, carries significant levels of shear. The contribution is dependent on the inclination and pattern of the shear crack. Specimens B10-R10-W20-S8 and B36-R10-W20-S8 showed steeper cracks (42° and 44°, respectively); therefore, the shear crack intersected two stirrups. The level of shear transferred by the stirrups is 12% for B10-R10-W20-S8 and 25% for B36-R10-W20-S8. A notable increase in the fraction of shear carried by transverse reinforcement occurs when the cracks show flatter inclination. Specimen B25-R10-W20-S8 exhibited a crack inclination of 36° that intersected four stirrups. The level of shear transferred by stirrups is 61% of the shear force at 99% of the ultimate strength. Similarly, the shear carried by this mechanism in the case of B25-R12-W20-S16 is 53% at 94% of the ultimate strength.

The interlocking between the protruding aggregates at the crack interface show various contributions depending on the crack width and slip, and the consequent contact phase. As the crack width increases (at subsequent loading stages) the contribution reduces. In the case of B25-R10-W20-S8, the measurement was taken at 99% of $V_{u,test}$ (w_{max} = 3.83 mm) (Fig. 12a); this mechanism contributes 6% to the shear transfer. In contrast, for smaller crack widths, either due to measurement at earlier loading stages (B10-R10-W20-S8) or absence of transverse reinforcement (B25-R10-W0-S8) the contribution is higher. Up to 28% of the shear

is carried by the aggregate interlock. The contribution is however modest, partly since the maximum aggregate used in this study was 10 mm (See Section 3.2.1 and Fig. 9a). On the other hand, the transfer of residual stresses through the crack interface is not assessed in this study as noted before, but this is expected to be negligible due to reduced dimensions of the fracture process zone. Accounting for a maximum crack width of w_{cu} = 0.16 mm for transfer of the residual stresses [38] for horizontal crack tips, the shear carried by this mechanism would be below 1 kN.

Besides its implicit contribution to the moment and shear capacity, the shear-key acts as support for the governing strut. In some cases, the opening of the governing shear crack produces free body rotation that results in slipping behaviour between the surrounding concrete and the shear-key. The assessment of this mechanism by means of simple shear-friction relationships show that a small fraction of shear is carried by this mechanism. The contribution varies between 3% and 15% (B25-R10-W20-S8, B10-R10-W20-S8, B36-R10-W20-S8 and B25-R12-W20-S16) and depends on the position of the shear cracks to the tip of the bottom flange of the shear-key. For B25-R10-W0-S8, the shear crack developed below the shear-key, and hence this mechanism was not activated.

The dowel bending is one of the principal shear transfer mechanisms for members without shear reinforcement (i.e. B25-R20-W0-S8). The shear carried by this mechanism is 47%, accounting for the secondary dowel mechanisms. This is backed up by small dowel spans and low stresses in the dowel. On the other hand, for large dowel spans (i.e. B10-R10-W20-S8) the contribution is 1%, and for high stresses in the dowel it is nearly non-existent (under 1%). The behaviour of the dowel is also heavily influenced by the thickness of the concrete cover. In this study, the actual cover exceeded 40 mm, therefore the bending of the dowel was restrained up to large applied loads.

The sum of the contributions of each shear transfer mechanism remains under that recorded by means of the load cell during testing ($\Sigma V_i < V_{i,test}$). At early loading stages, the results show higher contribution of the aggregate interlock because the aggregates are in the growing contact phase (crack width and slip within the limits to assure contact). The contribution of the mechanism decreases once the cracks widen and contact between aggregates is lost. The dowel action is significant in case of low stresses in the dowel and small dowel spans. Once these values increase, the dowel action becomes non-existent (i.e. in B25-R10-W20-S8). Secondary dowel mechanisms (cone breakout or concrete splitting) can be accounted for when the measurements are made at ultimate state (i.e. B25-R10-W0-S8).

The shear carried by the compressive zone decreases with increasing load and becomes minimal for low positions of the neutral axis. At early loading stages, a large fraction of the shear is transferred through the compressive zone. The contribution of the transverse reinforcement can be extensive when the failure is governed by large crack widths and stresses in the stirrup exceed the yield strength. The shear transfer due to composite slip is considered as a secondary mechanism in this study. It depends on the governing shear crack path and its relation to the flange-tip of the shear-key. A clear contribution of this mechanism would be observed when failure occurs due to crushing of the governing strut. On the other hand, for cracks developing in the outer connection area, the contribution is negligible.

4.2. Predictions of codified approaches

At present, no specific design provisions are available for assessing the shear capacity of hybrid RC beam/steel column configurations of the type examined in this study. The design of such hybrid forms is not directly covered by any of the existing
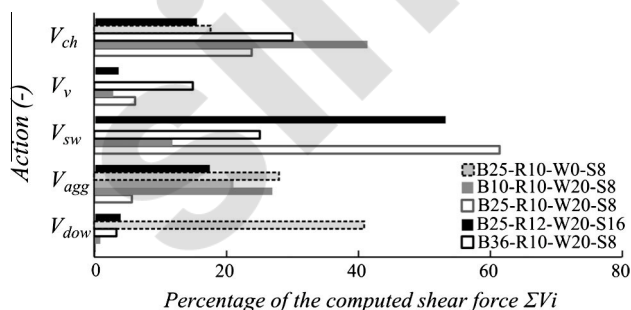

Fig. 16. Comparative contributions of shear transfer mechanisms.

procedures. These systems are not conventional RC structures as covered by Eurocode 2:2004 [39] or ACI318-08 [40], nor traditional composite steel–concrete members treated in Eurocode 4:2004 [41] or AISC2010 [42]. However, the detailed assessment of shear transfer mechanisms (STM), described in this study, shows that the shear failure modes exhibited by the specimens resemble those observed in reinforced concrete members. Accordingly, in the absence of specific guidance on hybrid components, the predictions of the expressions available in Eurocode 2 [39], ACI318-08 [40] and fib Model Code 2010 (Level 3 Approximation) [43] are examined and compared with those from the STM assessment. Additionally, a cumulative method that accounts for summed contributions of concrete and transverse reinforcement, to the shear strength of a hybrid member, is proposed below.

According to Eurocode 2 [39] provisions, the shear strength of a reinforced concrete member without shear reinforcement is dependent on the concrete strength f_c, flexural reinforcement ratio ρ_l and the size effect k (Eq. (17a)). On the other hand, the American code considers the shear strength to be dependent only on the compressive strength f_c (Eq. (17b)), whereas the fib Model Code offers three levels of approximation depending on the level of refinement required in design (Eq. (17c)). The shear strength depends on the k_v parameter defined by the angle of the critical shear crack θ_{cr}, longitudinal strain at mid-depth of the member ε_x and, for members without shear reinforcement, the maximum aggregate size d_g (Eq. (17d)).

$$V_{c,EC2} = 0.18(1 + \sqrt{200/d})(100\rho_l f_c)^{1/3} bd \tag{17a}$$

$$V_{c,ACI} = 0.17\sqrt{f_c} bd \tag{17b}$$

$$V_{c,MC2010} = k_v\sqrt{f_c} bz \tag{17c}$$

$$k_v = \begin{cases} [0.4/(1+1500\varepsilon_x)] \cdot [1300/(1000+0.7k_{dg}z)] \rightarrow \rho_w = 0 \\ 0.4/(1+1500\varepsilon_x) \rightarrow \rho_w \geqslant 0.08 f_c^{1/2}/f_{ys} \end{cases} \tag{17d}$$

In case of members requiring shear reinforcement, Eurocode 2 [39] accounts only for the transverse bars crossing the governing shear crack θ_{cr}, their geometry and yield strength (Eq. (18a)). ACI318-14 [40] and MC2010 LoA3 [43] consider a cumulative contribution (Eq. (18b)) between Eqs. (17b) and (18c) and Eqs. (17c) and (18d), respectively. In both codified provisions the contribution of transverse bars is function of geometry and yield strength. Limitations exist for the yield strength considered in ACI318-14 [40] ($f_{yw,eff}$ = 420 MPa) and Eurocode2 ($f_{yw,eff}$ = 0.8f_{yw}).

$$V_{sw,EC2} = \frac{A_{sw}}{s_w} z f_{yw} \cot\theta_{cr} \tag{18a}$$

$$V_R = V_c + V_{sw} \tag{18b}$$

$$V_{sw,ACI} = \frac{A_{sw}}{s_w} f_{yw} d \tag{18c}$$

$$V_{sw,MC2010} = \frac{A_{sw}}{s_w} z f_{yw} \cot\theta_{cr} \tag{18d}$$

The maximum shear strength in the presence of transverse reinforcement is dependent on geometry, angle of inclined struts and concrete strength (Eqs. (19a)–(19d)).

$$V_{max,EC2} = 0.5vbz f_c \sin 2\theta_{cr} \tag{19a}$$

$v = 0.6$ for normal strength concrete

$$V_{max,ACI} = 0.83\sqrt{f_c} bd \tag{19b}$$

$$V_{max,MC2010} = 0.5k_c bz f_c \sin 2\theta_{cr} \tag{19c}$$

$$k_c = 0.55(30/f_c)^{1/3} \leqslant 0.55 \tag{19d}$$

Inclination angles of the governing shear crack can be computed on the basis of the rearranged Eq. (19a) (see Eq. (20a)) for EC2 [39] provisions and according to Eq. (20b) in the case of Level III of Approximation of Model Code 2010 [43].

$$\theta_{cr,EC2} = 0.5\sin^{-1}[V_R/(0.5vbz f_c)] \tag{20a}$$

$$\theta_{cr,MC2010} = 29° + 7000\varepsilon_x \tag{20b}$$

In the current investigation, the yield strength obtained from material tests (f_{yw} = 592 MPa), the concrete strength assessed on cylinder material tests, and longitudinal strains ε_x, required for application of MC2010 LoA3 [43] provisions, as obtained from test measurements, were used. The effective crack inclinations θ_{cr} (as reported in Table 3) and those prescribed by design codes were accounted for in calculations.

The results in Table 5 show the shear strengths as predicted by the design codes, and Table 6 depicts the statistical parameters as the ratio between the strength obtained from tests and that predicted by Eqs. (17)–(20). The results of the shear transfer mechanism assessments (STM) are also reported in the same tables. The shear carried by the compressive zone, aggregate interlock, dowel action and composite slip are summed under the term V_c, and the contribution of stirrups is represented by V_{sw}. The predicted strengths are multiplied by a load proportionality factor λ that accounts for the ratio between the load at instrumented stages and $V_{u,test}$ ($\lambda_{B25-R10-W20-S8}$ = 0.99, $\lambda_{B10-R10-W20-S8}$ = 0.83, $\lambda_{B36-R10-W20-S8}$ = 0.90, $\lambda_{B25-R10-W0-S8}$ = 1.00, $\lambda_{B25-R12-W20-S16}$ = 0.94). Ratios between the test strength and those predicted exceeding unity represent conservative estimates ($\lambda V_{test}/\lambda V_{R,method}$ > 1), whereas values below unity represent unsafe estimates. Both the crack inclinations, as predicted by design codes and reported from the test programme, are used to enable a uniform and transparent comparison between codes and STM.

In the case of the specimen without transverse reinforcement, B25-R10-W0-S8, all codified predictions show safe estimates. Eurocode 2 [39] seem to show the highest accuracy, whereas Model Code 2010 (LoA3) [43] appears to be the most conservative. Predictions for members requiring transverse reinforcement provide conservative estimates of shear strength when the test shear crack inclinations are used for calculations. According to Table 6, the American design code shows the most accurate results both on average and coefficient of variance. When crack inclinations as predicted by codified provision are used for assessment, Eurocode 2 [39] shows better results (Avg. = 0.99, COV = 0.08). However, the code gives over conservative results for the member with long shear-key (l_v/h_v = 3.6) and unsafe values for the specimen with shortest embedment length (l_v/h_v = 1.0). Model Code 2010 (LoA3) [43] is able to predict most closely the phenomenological response of the specimens. The predicted crack inclinations are similar to those observed in tests. Consequently, the statistical parameters resulting from using $\theta_{cr,test}$ and $\theta_{cr,code}$, show more uniform predictions when compared to Eurocode 2 [39]. Overall, based on the average values and variance, all codified provisions seem to provide over-conservative estimations for Specimen B36-R10-W20-S8 (l_v/h_v = 3.6). It can be also be observed that the accuracy increases with the reduction in embedment length l_v (Table 6).

The STM assessment shows the smallest variance between the results. A detailed comparison between the results of the codified

Table 5
Strength predictions for tested specimens and results from the detailed assessment.

Specimen	Strength	EC2 $\theta_{cr,test}$	EC2 $\theta_{cr,code}$	ACI318	MC-LoAIII $\theta_{cr,test}$	MC–LoAIII $\theta_{cr,code}$	STM	Eqs. (22a)–(22c)	$\lambda_{Bi} V_{i,test}$*
B25-R10-W0-S8	$\lambda_{Bi}V_c$*	**143**	–	**135**	**98**	–	**152**	**169**	**175**
B10-R10-W20-S8	V_c	–	–	130	105	105	193	141	**268**
	V_{sw}	162	364	162	162	196	32	135	
	$\lambda_{Bi}V_R$*	**134**	**302**	**243**	**222**	**250**	**225**	**229**	
	$\lambda_{Bi}V_{max}$*	894	620	529	769	740	–	634	
B25-R10-W20-S8	V_c	–	–	147	103	103	126	179	**351**
	V_{sw}*	202	366	163	202	185	216	168	
	$\lambda_{Bi}V_R$*	**199**	**362**	**307**	**302**	**285**	**342**	**343**	
	$\lambda_{Bi}V_{max}$*	1287	933	710	1026	1050	–	901	
B36-R10-W20-S8	V_c	–	–	137	113	113	248	207	**356**
	V_{sw}*	151	364	162	151	198	89	126	
	$\lambda_{Bi}V_R$*	**136**	**328**	**269**	**237**	**280**	**337**	**299**	
	$\lambda_{Bi}V_{max}$*	1067	736	600	890	849	–	745	
B25-R12-W20-S16	V_c	–	–	123	102	76	125	148	**327**
	V_{sw}	188	354	158	188	167	194	157	
	$\lambda_{Bi}V_R$*	**177**	**333**	**264**	**248**	**228**	**325**	**286**	
	$\lambda_{Bi}V_{max}$*	945	678	564	799	821	–	621	

Note: numbers shown in bold depict the governing shear strength assessed by Eqs. (17)–(22), STM and test shear strength, and modified by the load proportionality factor λ_{Bi}.
 * All values in kN, Load Proportionality Factor – λB25-R10-W0-S8 = 0.94, λB10-R10-W20-S8 = 0.83, λB25-R10-W20-S8 = 0.99, λB36-R10-W20-S8 = 0.90, λB25-R12-W20-S16 = 1.00.

Table 6
Comparison between code predictions, STM assessments and test results.

Member without transverse reinforcement						
$\lambda V_{i,test}/\lambda V_{Rmethod}$	EC2	ACI318	MC2010-LoAIII		STM	Eqs. (22a)–(22c)
B25-R10-W0-S8	**1.23**	**1.29**	**1.78**		**1.15**	**1.03**

Members with transverse reinforcement						
$\lambda V_{i,test}/\lambda V_{Rmethod}$	EC2 $\theta_{cr,test}$	EC2 $\theta_{cr,code}$	ACI318	MC2010-LoAIII $\theta_{cr,test}$	MC2010-LoAIII $\theta_{cr,code}$	STM	Eqs. (22a)–(22c) $\theta_{cr,test}$
B10-R10-W20-S8	1.99	0.89	1.10	1.21	1.07	1.19	1.17
B25-R10-W20-S8	1.76	1.02	1.15	1.16	1.23	1.03	1.02
B36-R10-W20-S8	2.62	1.09	1.33	1.50	1.27	1.06	1.19
B25-R12-W20-S16	1.85	0.98	1.24	1.32	1.43	1.07	1.14
Average	**2.05**	**0.99**	**1.20**	**1.30**	**1.25**	**1.09**	**1.13**
COV	**0.19**	**0.08**	**0.08**	**0.12**	**0.12**	**0.06**	**0.07**

Note: numbers shown in bold in the table illustrate statistical parameters grouped per category.

provisions and the shear transfer actions STM assessment of all tested specimens is plotted in Fig. 17a–c. The comparison is made with respect to the total reinforcement ratio ρ_{tot} that accounts for the presence of the shear-key and its embedment length in the member (Eq. (21)). Based on the plot trend lines, it can be observed that all design codes show a tendency of over-estimating the shear strength for members with long embedded shear-keys. Considering that for the STM assessment, the term V_c in Table 5 includes the cumulative contribution of aggregate interlock, dowel action, composite slip and transfer through compressive zone, it can be observed that when compared to codified provisions the results seem to be conservative. On the other hand, the contribution of transverse reinforcement V_{sw} shows scatter since for intermediate embedment lengths (l_v/h_v = 2.5) it is underestimated and for the extreme cases (i.e. l_v/h_v = 1.0 and l_v/h_v = 3.6) it is conservative.

4.3. Predictions of proposed method

The following section introduces a method to assess the shear strength of hybrid members locally provided with shear-keys as those described in Section 2 of the paper. Test observations and STM assessments are used as a basis for modification of Eqs. (17a)–(17d) in order to account for the contribution and influence of the shear-key on the shear strength of the members. The rationale behind the method proposed in Eqs. (21) and (22) is to account for a cumulative contribution of the shear transfer through the compressive zone, aggregate interlock, dowel action and composite slip, grouped under the term V_c, and separately, for the contribution of the transverse bars V_{sw}. The strength of a hybrid member is given by the sum of the two terms $V_R = V_c + V_{sw}$ (Eq. (18b)).

The presence of a steel beam in a reinforced concrete member increases locally the strength and stiffness. The behaviour in the shear-key region is similar to a fully encased composite member. When the member is subjected to flexural and shear action, the neutral axis drops towards the extreme compressed fibre. Consequently, the flexural reinforcement bars and part or the entire shear-key are in tension. Strain gauge records showed levels of about 75% of the yield strain on the top flange of the shear-key. Fig. 13 emphasizes the sectional equilibrium of the composite region of the hybrid member. The plastic moment of the composite section is dependent on the lever arms z_1 and z_v and cross-sectional characteristics of the reinforcing steel (flexural bars and shear-key). Implicitly, the stiffness response of the member is dependent on the shear-key section size and amount of flexural reinforcement.

In fully composite members, the presence of the steel member contributes to the total reinforcement ratio of the member (Eq. (21a)). However, the presence of the steel element is local within the length of the member. Hence, its influence on the ultimate strength is dependent on its embedded length (increase in strength with increase in embedded length as depicted in Fig. 3 and Table 3). This aspect is captured by multiplying the contribution of the shear-key to the total reinforcement ratio with a factor λ_v
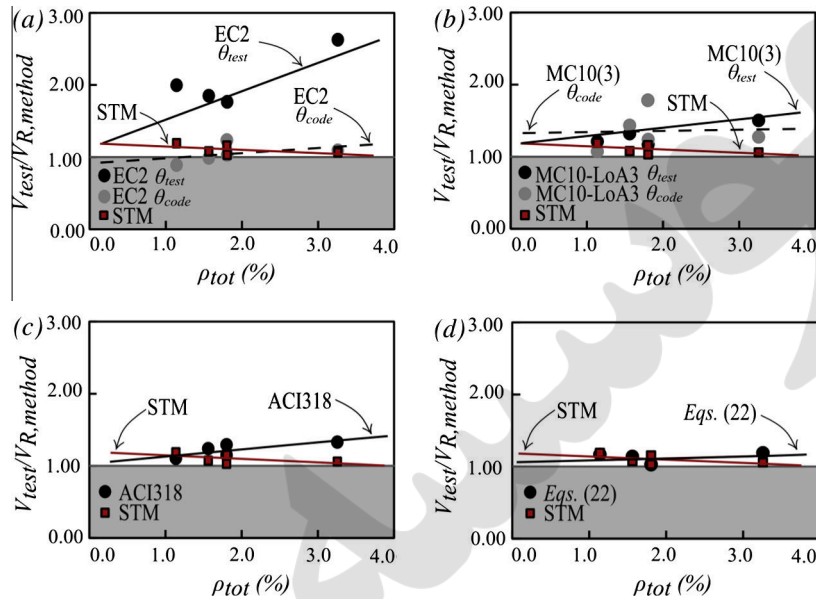
Fig. 17. Comparison between estimated shear transfer (STM) and codified predictions (a) Eurocode 2, (b) Model Code 2010 LoA3, (c) ACI318; (d) Comparison between estimated shear transfer (STM) and proposed Eq. ((22)).

that depends on the embedded length l_v which is related to the half-span of the member r_s (Eq. (21b)). The total reinforcement ratio is embedded in Eq. (22a) for shear strength assessment of hybrid members without transverse reinforcement.

For the configuration considered, based on limit analysis, the position of the neutral axis is found to be in the region of the bottom flange of the composite region and in a lower position in the conventional RC case. As observed in the tests, failure occurs at the interface region where the neutral axis is found to be mid-way between the two. The lever arm accounted for in shear calculations (i.e. $z = 0.9d$) in typical reinforced concrete members, seems to be slightly higher than that in the hybrid members investigated here. Hence, a representation of the lever arm corresponding to 75% of the effective depth leads to a more satisfactory estimation of the contribution of the stirrups to shear strength of hybrid members with transverse reinforcement (Eq. (22b)). The shear strength of hybrid members with transverse reinforcement is given by the cumulative contribution of Eqs. (22a) and (22b).

When crushing failure occurs, the governing strut is supported on the bottom flange of the shear-key. Therefore, the vertical projection of the strut reduces when compared to a typical RC member. Similar to the case when the contribution of the transverse reinforcement is estimated, the lever arm z, as typically used for RC members is reduced. In the case of shear failure resulting from strut crushing, the 'hybrid' lever arm z_v becomes the distance between the top face of the bottom flange of the shear-key and the centroid of the longitudinal reinforcement (Fig. 13 and Eq. (22c)).

The governing shear crack inclinations observed during the tests vary between 36 to 44 degrees. In design, crack inclinations should be determined starting from elastic stress distribution (45°) which will give the most conservative result since the number of transverse bars intersected by the crack is minimal or, by accounting for a compatible strut and tie mechanism considering that the governing strut is supported by the tip of the shear-key and joins the first stirrup located at a distance equal or higher than 0.75d from the tip of the shear-key. Alternatively, the semi-empirical Eq. (22d) adapted from [44] by considering the test results reported in Table 3 could be used to assess the inclination of the governing shear crack.

$$\rho_{tot} = \rho_l + \lambda_v \rho_v \tag{21a}$$

where $\lambda_v = (l_v/r_s)^3$ (21b)

and $\rho_v = A_v/(b_c d_v)$ (21c)

$$V_{c,prop} = 0.18(1 + \sqrt{200/d})\left[100\ \rho_l + \rho_v\left(\frac{l_v}{r_s}\right)^3\right)f_c\right]^{1/3} bd \tag{22a}$$

$$V_{sw,prop} = 0.75d\frac{A_{sw}}{s_w}f_{yw}\cot\theta_{cr,prop} \tag{22b}$$

$$V_{max,prop} = 0.5\nu b z_v f_c \sin 2\theta_{cr,prop} \tag{22c}$$

$$\tan\theta_{cr,prop} = 0.6 + \rho_{tot}\frac{f_{ys}}{f_c}\left(\frac{d}{1600}\right)^{1/2} \text{ and } \frac{2}{3} \leqslant \tan\theta_{cr,prop} \leqslant 1 \tag{22d}$$

Tables 5 and 6 and Fig. 17d depict the strength estimations using Eqs. (22a) and (22b), and the shear crack inclinations observed in tests and reported in Table 3. The influence of the shear-key on the shear strength is accounted for by a series of modifications to Eqs. (17a)–(17c) as result of test observations and STM assessments. In the case of the member without transverse reinforcement and intermediate embedment length of the shear-key, the proposed method shows the best estimation when compared to codified provisions ($\lambda V_{test}/\lambda V_{R,Eq.22} = 1.03$). In the case of members provided with transverse reinforcement, the prediction is more uniform showing lower scatter between results (Average = 1.13 and COV = 0.07). The comparison between the STM, codified approaches and proposed Eq. (22) illustrate that conventional reinforced concrete code approaches tend to provide over-conservative predictions for both relatively high and relatively low total reinforcement ratios. In contrast, the assessments based on the proposed modified expressions in Eq. (22) offer more realistic predictions, and are able to capture faithfully the influence of the embedded length of the shear-key on the ultimate shear strength for hybrid members of the type investigated in this paper.

The predicted results show good agreement with those obtained from tests for members with various shear-key embedment lengths ($l_v/h_v = 1.0$–3.6), with stiffness ratios that involve rigid behaviour of the shear-key, using normal concrete, and provided with intermediate flexural reinforcement ratios for the bare

reinforced concrete region. More conservative estimations could be obtained if design safety factors are used. Overall, short embedment lengths of the shear-key seem to be more effective from the practical point of view. A ratio of $l_v/h_v = 1.0$ appears to be sufficient to ensure a smooth transfer of forces between the reinforced concrete beam and steel column, and a stiff response of the shear-key. The structural response of a hybrid member with a short shear-key resembles a typical reinforced concrete member, hence may be a desirable solution in practice.

5. Concluding remarks

This paper focuses on examining the fundamental shear transfer mechanisms in hybrid structural systems consisting of reinforced concrete beams connected to steel columns by means of embedded shear-keys. A full account of the results of a series of five large scale tests on hybrid reinforced concrete beam-to-steel column assemblages is presented. In addition to providing detailed test results which can be used for future complementary studies, the experimental findings provide an in-depth insight into the contributions of various shear transfer mechanisms. Based on detailed measurements of crack growth and propagation at various load levels approaching failure, the contribution of each shear transfer mechanism to the ultimate shear strength is quantified. It is shown that the behaviour at ultimate shear strength of the hybrid members is characterised by the development of a governing shear crack in the vicinity of the tip of the bottom flange of the shear-key. The ultimate shear strength is primarily dependent on the embedded length of the shear-key, reinforcement layout and ratios, and the concrete strength. The typical shear failure of hybrid members resembles that of reinforced concrete elements: crushing of the governing strut (supported by the bottom flange of the shear-key) or diagonal tension (controlled failure in the presence of transverse reinforcement). At loading stages prior to ultimate limit state, the main benefit from the presence of the embedded shear-keys is that it shifts the weak section away from the maximum demand region, both in terms of bending moment and shear (for continuous beams), hence delaying the failure.

The study illustrates that analytical models for predicting the contribution of shear transfer mechanisms can be adopted to assess the shear strength by means of detailed measurements of crack patterns and kinematics. The summed contribution of all shear transfer mechanisms shows close agreement, within a coefficient of variation of 6%, with the recorded shear force during the tests for members with transverse reinforcement. Before reaching the ultimate limit state, shear is carried by a combination of aggregate interlock, dowel action, stirrups and the compressive zone. Their magnitude is highly influenced by the applied load and consequently by the crack pattern, width and slip. Secondary shear transfer mechanisms such as composite action between the shear-key and the concrete interface can contribute up to 15% of the total shear transfer. The crack inclination also influences the contribution of each transfer mechanism. For flatter cracks, the contribution of the transverse reinforcement is significant, whereas the aggregate interlock provides a comparatively lower contribution. On the other hand, for steeper cracks the number of transverse bars intersected is reduced and their contribution is consequently smaller, whereas the aggregate interlock contribution is higher. In the case of specimens without shear reinforcement, the main transfer mechanisms are the aggregate interlock and dowel actions since the stresses in the dowel remain at low levels at failure. The crack inclinations observed in tests vary from 36° to 44°.

Using the experimental results and observations, the paper also assesses the adequacy of strength predictions obtained from analytical models which are adopted in the design of conventional reinforced concrete members, with emphasis on European and North American provisions. It is shown that these procedures can be used to provide overly conservative predictions for evaluating the shear strength of hybrid members. An analytical approach is therefore proposed in order to provide a more realistic prediction of the ultimate shear behaviour of hybrid members of the form investigated in this paper. The suggested procedure accounts for the influence of the characteristics of the shear-keys on the ultimate shear strength, and offers a more realistic prediction of the behaviour in comparison with conventional reinforced concrete design provisions.

References

[1] Harries KA, Gong B, Shahrooz BM. Behaviour and design of reinforced concrete, steel and steel–concrete coupling beams. Earthquake Spectra 2000;16(4) [November].
[2] Gong B, Shahrooz BM. Concrete–steel composite coupling beams, I: component testing. J Struct Eng 2001;127(6):625–31.
[3] Shahrooz BM, Gong B, Tunc G, Deason JT. An overview of reinforced concrete core wall-steel frame hybrid structures. Prog Struct Eng Mater 2001;3:149–58.
[4] Su RKL, Lam WY, Pam HJ. Experimental study of plate-reinforced composite deep-coupling beams. Struct Design Tall Spec Build 2009;18:235–57.
[5] Sheikh TM, Deierlein GG, Yura JA, Jirsa JO. Beam–column moment connections for composite frames: Part 1". J Struct Eng 1989;115(11):2858–76.
[6] Chou CC, Uang CM. Cyclic performance of a type of steel beam to steel-encased reinforced concrete column moment connection. J Constr Steel Res 2002;58:637–63.
[7] Cheng CT, Chen CC. Seismic behavior of steel beam and reinforced concrete column connections. J Constr Steel Res 2005;61:587–606.
[8] Lee CH, Kim JW, Song JG. Punching shear strength and post-punching behavior of CFT column to RC flat plate connections. J Constr Steel Res 2008;64:418–28.
[9] Kim JW, Lee CH, Kang THK. Shearhead reinforcement for concrete slab to concrete-filled tube column connections. ACI Struct J 2014;111(3) [May–June].
[10] Eder MA, Vollum RL, Elghazouli AY. Performance of ductile RC flat slab to steel column connections under cyclic loading. Eng Struct 2012;36:239–57.
[11] Eder MA, Vollum RL, Elghazouli AY. Inelastic behaviour of tubular column-to-flat slab connections. J Constr Steel Res 2011;67:1164–73.
[12] Bompa DV, Elghazouli AY. Force transfer mechanisms between steel columns and RC beams by means of shearkeys. In: Proceedings of eurosteel 2014 conference; 2014.
[13] Kani GNJ. Basic facts concerning shear failure. ACI J Proc 1966;63(3):675–92.
[14] Taylor HPJ. The fundamental behaviour of reinforced concrete beams. In: Bending and Shear. ACI Special Publication SP42-3; 1974. p. 43–77.
[15] Taylor HPJ. Further tests to determine shear stresses in reinforced concrete beams. Technical Report, TRA 438. Cement and Concrete Association UK; February 1970.
[16] Walraven JC, Reinhard HW. Theory and experiments on the mechanical behaviour of cracks in plain and reinforced concrete subjected to shear loading. Heron 1981;26(1a):5–68.
[17] Walraven JC. Aggregate interlock: a theoretical and experimental analysis, Technical Report 1628-481-7. Delft University Press; 1980.
[18] Paulay T, Loeber PJ. Shear transfer by aggregate interlock, ACI Special Publication SP-42, vol. 42, p. 1–16, http://dx.doi.org/10.14359/17277.
[19] Dei Poli S, Gambarova PG, Karakoc C. Aggregate interlock role in RC thin-webbed beams in shear. J Struct Eng ASCE 1987;113(1) [January].
[20] Dei Poli S, Di Prisco M, Gambarova P. Shear response, deformations, and subgrade stiffness of a dowel bar embedded in concrete. ACI Struct J 1992;89(6):665–75.
[21] Swamy RN, Qureshi SA. An ultimate shear strength theory for reinforced concrete T beams with web reinforcement. ICE Proc 1974;57(1):21–34.
[22] Swamy RN, Andriopoulos AD. Contribution of aggregate interlock and dowel forces to the shear resistance of reinforced beams with web reinforcement ACI Special Publication SP42-6; 1975. p 129–66.
[23] Chana PS. Analytical and experimental studies of shear failures in reinforced concrete beams. Proc Inst Civ Eng Part 1988;2(85):609–28 [December].

[24] Chana PS. Investigation of the mechanism of shear failure of reinforced concrete beams. Mag Concr Res 1987;39(141) [December].

[25] Sagaseta J, Vollum RL. Influence of aggregate fracture on shear transfer through cracks in reinforced concrete. Mag Concr Res 2011;63(2):119–37.

[26] Campana S, Fernández Ruiz M, Anastasi A, Muttoni A. Analysis of shear-transfer actions on one-way RC members based on measured cracking pattern and failure kinematics. Mag Concr Res 2013;56(6):386–404 [UK].

[27] Wium JA. A composite columns: force transfer from steel section to concrete encasement. PhD Thesis Swiss Federal Inst. of Tech., Lausanne, Switzerland; 1992.

[28] Wium JA, Lebet JP. Simplified calculation method for force transfer in composite columns'. J Struct Eng 1994;120(3):728–46.

[29] Roeder CW, Chmielowski R, Brown CB. Shear connector requirements for embedded steel sections. J Struct Eng 1999;125(2):142–51.

[30] Mattock H. Shear transfer in reinforced concrete – recent research. PCI J 1972 [March].

[31] Ulaga T. Betonbauteile mit Stab und Lamellenbewehrung: Verbund- und Zuggliedmodellierung. Doctorate thesis ETH Zürich Nr 2003;15062.

[32] Guidotti R. Poinçonnement des planchers-dalles avec colonnes superposées fortement sollicitées. EPF Lausanne, Doctorate thesis 2010;4812.

[33] Soroushian P, Obaseki K, Rojas M. Bearing strength and stiffness of concrete under reinforcing bars. ACI Mater J 1987;84(3):179–84 [May–June].

[34] Dulacska H. Dowel action of reinforcement crossing cracks in concrete. ACI J, Proc 1972;69(12):754–7 [December].

[35] Mirazei Y. Post-punching behaviour of reinforced concrete slabs. Doctorate thesis, EPFLausanne, No. 4613; 2010.

[36] Hsu TTC, Mau ST, Chen B. Theory on shear transfer strength of reinforced concrete. ACI Struct J 1987;84(2):149–60 [March–April].

[37] Hsu TTC. Softened truss model theory for shear and torsion. ACI Struct J 1988:624–35 [November–December].

[38] Hillerborg A. Analysis of crack formation and crack growth in concrete by means of fracture mechanics and finite elements. Cem Concr Res 1976;6:773–82.

[39] EN 1992-1-2 – Eurocode 2: Design of concrete structures – Part 1: General rules and rules for buildings. European Committee for Standardization, Brussels; December 2004.

[40] ACI 318M-08 building code requirements for structural concrete (ACI 318M-08) and Commentary American Concrete Institute; June 2008.

[41] EN 1994-1-1 Eurocode 4: design of composite steel and concrete structures – Part 1–1: general rules and rules for buildings. Brussels: European Committee for Standardization; December 2004.

[42] AISC. Specification for Structural Steel Buildings, (ANSI/AISC 360-10). Chicago, IL: American Institute of Steel Construction; 2010.

[43] Model Code 2010 – final draft, vol. 1 & vol. 2, fib Bulletins 65 & 66, March 2012, Lausanne.

[44] Bompa DV, Oneţ T. Punching shear strength of RC flat slabs at interior connections to columns. Mag Concr Res, http://dx.doi.org/10.1680/macr.14.00402.